# Formation and Characteristics of Microstructures from PEM Fuel Cell Catalyst Ink Drying

by

**Jingyi Wang**

A thesis

presented to the University of Waterloo

in fulfillment of the

thesis requirement for the degree of

Master of Applied Science

in

Mechanical Engineering

Waterloo, Ontario, Canada, 2015

I hereby declare that I am the sole author of this thesis. This is a true copy of the thesis, including any required final revisions, as accepted by my examiners.

I understand that my thesis may be made electronically available to the public.

Jingyi Wang

# Abstract

In this study, the process of catalyst ink drops drying in room air is investigated experimentally, which is key to the fabrication of, hence the microstructure formation in, the catalyst layers of polymer electrolyte membrane fuel cells (PEMFCs). State-of-the-art catalyst layer in PEMFCs is typically made through the drying of catalyst ink, which is a solvent based colloidal solution with suspended aggregates of nano catalyst particles supported on meso carbons (e.g. C/Pt) and perfluorosulfonic polymer (e.g. Nafion®). Catalyst ink samples are prepared using various Nafion loadings while the C/Pt loading and solid content (C/Pt and Nafion) are held constant. The real-time drying process is observed through an optical microscopy and the dried deposition is investigated with a scanning electron microscopy (SEM) and the optical microscopy. The dried pattern characterizations show the C/Pt agglomerates are more uniformly deposited as the Nafion loading is increased: the deposition at the edge becomes thicker and wider; unique pedal-like pattern with uniform distance is aligned along the inner side of the thicker edge; and the microstructure pattern transits from the concentric rings toward the drop center to heterogeneously detached aggregations. As the Nafion loading is increased, the evaporative cooling induced thermo-capillary flow in the drop varies significantly, from convective outward flow combining with Bernard-Marangoni cell at the center of the drop, to reversed flow coupling with three-dimensional thermo-capillary waves in the annular region near the edge of the drop, which dictates C/Pt agglomerates transport and leads to varies deposition. This study provides insight into the fundamental understanding of complex drying dynamics during catalyst ink drying, and laid theoretical foundation for further studies on achieving CL microstructure with increased catalyst utilization.

# Acknowledgements

I would like to express my gratitude to my advisor Dr. Xianguo Li for his guidance for my MASc study and writing of this thesis. I would also like to thank Dr. Fue-Sang Lien and Dr. Zhongwei Chen for taking the time to scrutinize my thesis.

A sincere thank you to Dr. Yongxin Wang for the time we spent discussing the possible research plan. I would also like to thank Gaopeng Jiang for his patience in explaining related chemical knowledge and help in use of experimental facilities. My thanks also goes to other colleagues in my lab, Andy Shen, Garrett Gauthier, Abbas Ghasemi, Yanzhou Qin, Grant Unsworth, and Aaron Pereira, Samane Shahgaldi, Ibrahim Alaefour, for their stimulating discussions.

I would also like to say thank you to all of my friends who surround and share laughter and tears with me, which makes my life in Waterloo full of memory.

I also have to show my deepest gratitude to my parents who gave birth to me at the first place and for their continuous support and love without expecting any return.

Finally, I give thanks to God for the continuous guidance and discipline all the way along and throughout the rest of my life.

# Contents

# List of Figures

# List of Tables

# Nomenclature

PEMFC   Polymer electrolyte membrane fuel cell

CL      Catalyst layer

MEA     Membrane electrode assembly

GDL     Gas diffusion layer

CCM     Catalyst coated membrane

PEM     Polymer electrolyte membrane

CCL     Cathode catalyst layer

ACL     Anode catalyst layer

HOR     Hydrogen oxidation reaction

ORR     Oxygen reduction reaction

SEM     Scanning electron microscopy

$J$     Evaporative flux

NFP     The weight percentage of Nafion in all the solid content (Nafion and C/Pt)

$K^{-1}$   Capillary length of fluid

# Chapter 1 Introduction

1.1 Background

Polymer electrolyte membrane fuel cells (PEMFCs) have reached its pre-commercial stage with further target on cost reduction and durability improvement [1, 2]. To be commercially viable, automotive and stationary PEMFCs must achieve a competitive performance and durability at an affordable cost while matching the obligatory output power requirement. For example, the Department of Energy (DOE) has set durability targets of 5000 hours for automotive applications with cost of \$30/kw, and 40,000 hours for 1 to 10 kW stationary applications with cost of \$750/kW under realistic operating conditions including stop/start, low power, idling, dynamic operation, and sub-zero start-up by 2015 [3]. State-of-the-art catalyst layers (CLs) employ Pt supported on carbons (e.g. C/Pt) as the catalyst for electrochemical reaction [4]. Studies on CLs have been drawing cooperative research efforts in the fields of material science [5], structural optimization simulation [6], advanced techniques for microstructure characterization [7], and many others [2]. The high production cost (the material cost, e.g. precious metal for catalyst, and fabrication cost), which accounts for 49 % of the total production cost with a production rate of 500,000 systems/year [1], and limited durability of CLs has been the greatest hurdle for PEMFCs commercialization [8].

1.2 Operational principle of PEM fuel cells

A schematic of a PEMFC unit and its operational principle are shown in Fig. 1.1. The membrane electrode assembly (MEA) is a sandwiched structure composed of electrodes (anode and cathode) made of gas diffusion layers (GDLs) and catalyst layers (CLs), and one polymer electrolyte membrane (PEM). The CL are further differentiated as cathode CL (CCL) and anode

CL (ACL), the CCL usually has higher platinum loading than the ACL. Shown in Fig. 1.1 (a), hydrogen gas enters into the anode flow channel and diffuses through the GDL into the ACL, where hydrogen molecules are decomposed into electrons and protons through hydrogen oxidation reaction (HOR):

$H_2 \rightarrow 2H^+ + 2e^-$

Protons migrate through the PEM, while electrons travel through the external circuit, then the two meet at the CCL again. Oxygen/air enters though the cathode flow channel and diffuses through the GDL, and reaches the CCL, and then combines with protons and electrons to generate water and heat according to oxygen reduction reaction (ORR) shown in Fig. 1.1 (b):

$\frac{1}{2} O_2 + 2 H^+ + 2e^- \rightarrow H_2O +$ Waste Heat
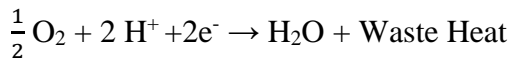
The whole cell reaction is written as: $\frac{1}{2} O_2 + H_2 \rightarrow H_2O +$ Waste Heat

Within this cell unit, the sandwiched structure composed of ACL, PEM, and CCL is usually called catalyst coated membrane (CCM). Figure 1.2 shows the dimension of a typical catalyst coated membrane (CCM) composed of three layers (CCL, PEM, and ACL) and with through-plane thickness between $10 - 50$ μm and in-plane length of several cm.

The I-V curve, or polarization curve, is the most important indicator for the PEMFCs performance in terms of systematic perspective shown in Fig. 1.3. The polarization curve is classified into three regions, activation, Ohmic, and concentration, as they are mainly responsible for the losses (polarizations) occurred in each region. The polarization is caused by a series of complex processes occurring in the cell unit, including reactant gas transport, migration and diffusion of protons and electrons, electrochemical reaction, and water transport by diffusion, permeation and vaporization or condensation [4].

(a)                                                    (b)
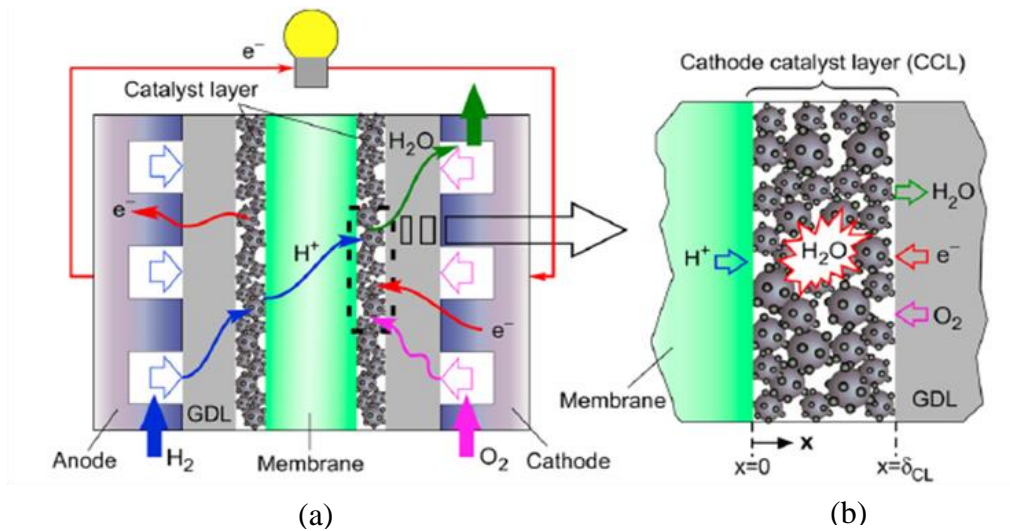
Fig 1.1. Schematic of the components of a PEMFC unit and its operational principle [9]. (a) The operational principle of PEMFC. (b) Oxygen reduction reaction (ORR).



(a)                                                    (b)
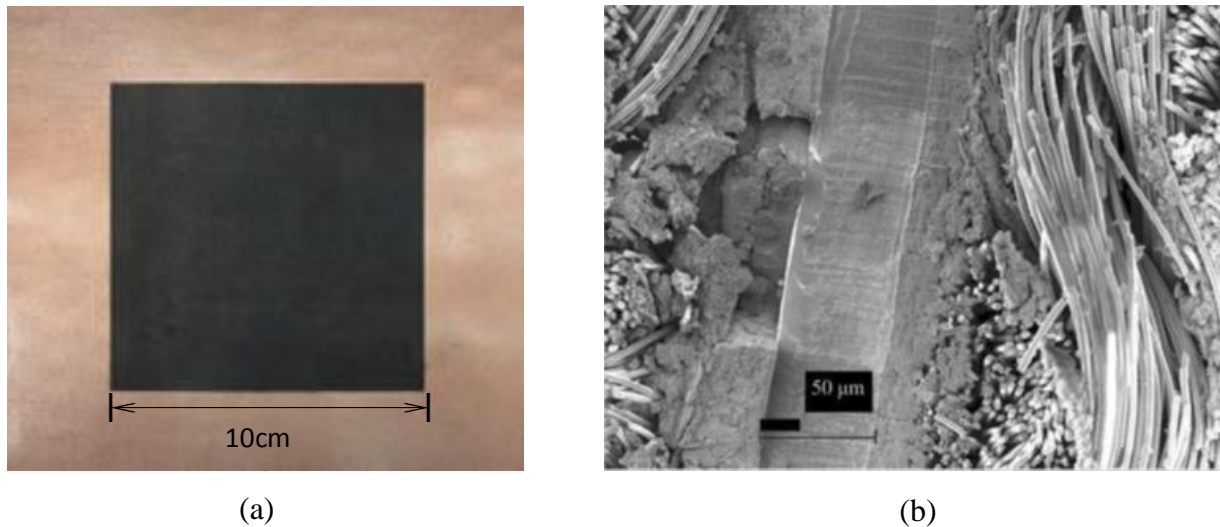
Fig 1.2. Typical dimensions of MEA. (a) Dimensions of catalyst layer (CL) used typically in laboratory study (b) SEM of membrane electrode assembly (MEA) [1].

Activation polarization is caused by sluggish reaction kinetics and low catalyst activity of the CL, and has a profound effect on the cell performance when the current density is low (e.g., < 0.1 A/cm$^2$). Ohmic polarization is attributed to the inconsistence between protons and electrons transport inside the cell. Concentration polarization is caused by the mass transport limitation of Reactant gas in reaching the reaction site, especially the CCL, at high current densities (e.g., >

---

[1] This image is taken by Yinqin Shen, another graduate student in the same research group.

0.5 A/cm$^2$). All the three polarizations are closely related to the microstructure of the CLs [4].
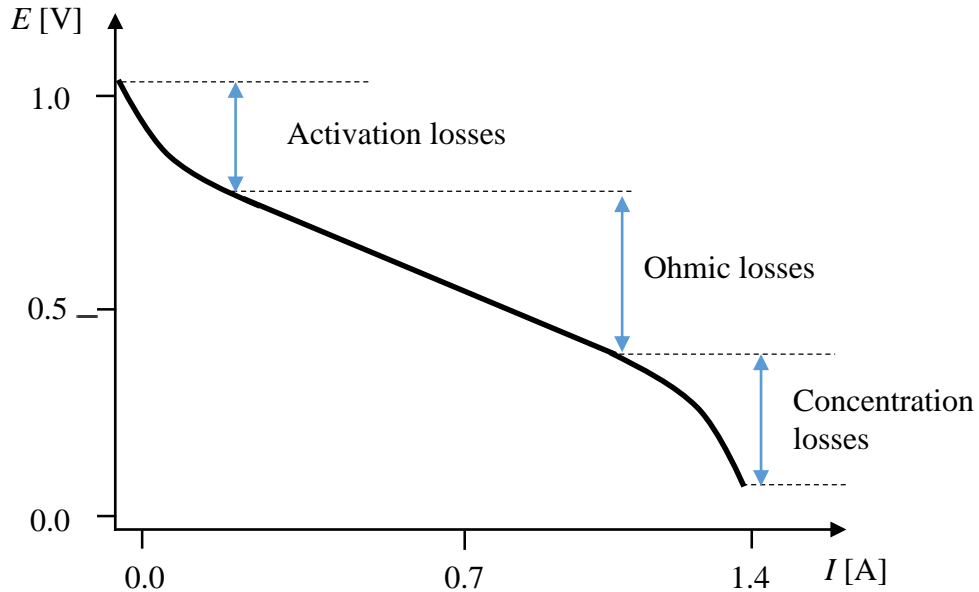


Fig 1.3. Schematic of a typical polarization curve of cell performance. E denotes the output voltage that the cell unit can provide, I denotes the output current. The output voltage, E, decreases as the current, I, drawn from the cell is increased, due to activation, Ohmic, and concentration polarizations [4].

## 1.3 Effect of microstructure of CL on catalyst utilization and durability

The limited catalyst utilization and durability of CL is closely related to its heterogeneous microstructure. State-of-the-art CLs employ Pt supported on carbons (C/Pt), and perfluorosulfonic polymer, e.g. Nafion polymer, as ion conductors and binding agent [10]. Therefore, perfluorosulfonic polymer is also called ionomer. Figure 1.4 illustrates the heterogeneous porous structure of CL. Figure 1.5 illustrates the corresponding schematic of CL microstructure to give a clear view of the heterogeneous structure. The porous structure of CL covers a wide range of length scales, which spans from the carbon-supported catalyst particles (C/Pt) of 3-10 nm at the nano-scale, then to the C/Pt agglomerates of 100 − 300 nm due to binding effect of ionomer at meso-scale, then C/Pt agglomerates further form aggregates of 1 - 3 μm at micro-scale, and finally to the porous medium of CL with a through-plane thickness of 10 − 50 μm. Within agglomerates, meso-pores of 2 -20 nm exists; as the agglomerates coalesce into

4

aggregates, the secondary pores, pores network of > 20 nm, is formed in the interstices [11][12].
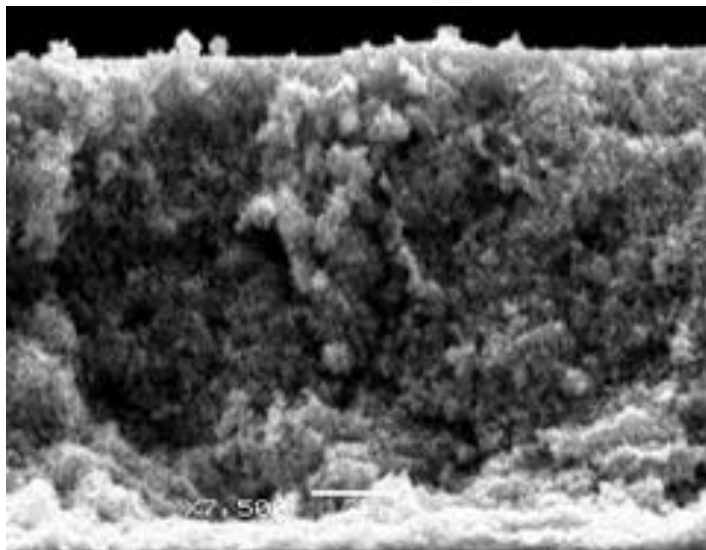


Fig 1.4. Cross sectional SEM image of catalyst coated membrane (CCM) shows the heterogeneous porous structure[2].



Carbon     Platinum Particle (Pt) (~ 2 nm)     100-300 nm        $1 - 3$ μm

Primary particle        C/Pt agglomates        Aggregates
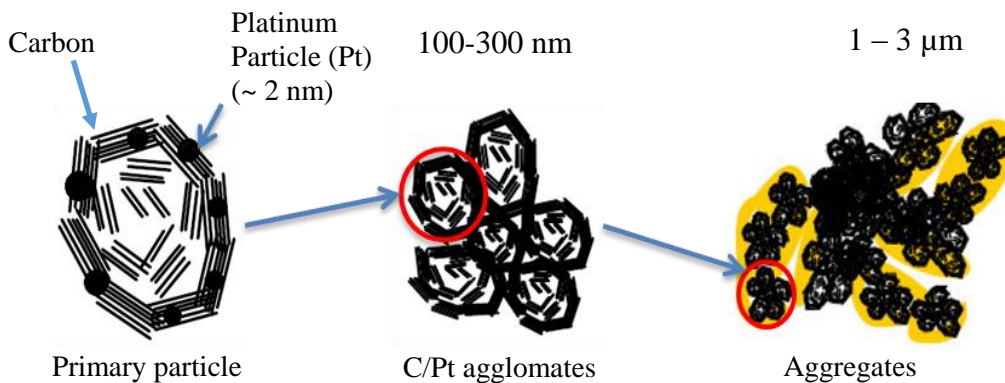
Fig 1.5. Schematic of the CL microstructure with a wide range of length scale [11][12].

1.3.1 Effect of microstructure on catalyst utilization

The heterogeneous porous structure of CL results in imbalanced porosity distribution and ionomer distribution, then affects both proton and electron conductivity as well as reactant gas transport, and eventually the electrochemical reaction in CL. The pivotal part of the CL is the triple phase boundary (TPB) where the ORR actually occurs as shown in Fig. 1.6. Oxygen can

---

[2] The image is taken by Yinqi Shen, another graduate student in the same research group.

reach the TPB via two passages, the pores within aggregates and the ionomer phase, while the protons reach the TPB via Nafion and electrons through the conducting carbon support and the platinum particles [15]. Therefore imbalanced distribution of porosity and ionomer leads to a consequence that platinum particles are not given equal chances of accessing oxygen, proton and electron, thus results in limited Pt utilization.
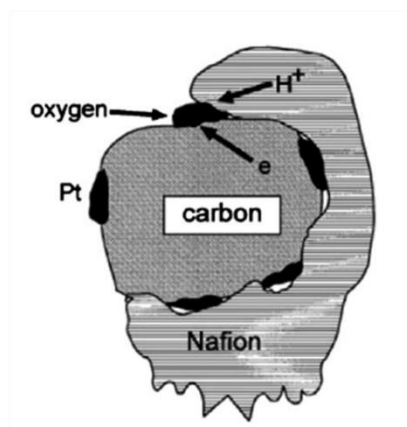


Fig 1.6. Schematic of triple phase boundary, where the electrolyte, catalyst, and reactants come into contact and the cell reactions actually occur [15].

1.3.2 Effect of microstructure on CL degradation

CL degradation has been identified as one significant factor for performance reduction, hence, degradation mechanisms and relevant mitigation strategies for degradation are increasingly drawing attention in many fields of research [16]. CL degradation refers to morphological deviation from fresh state after long hour operation, including cracks, delamination, catalyst shifting and clusters, carbon coarsening and corrosion, all leading to drastic performance drop [17]. Several key factors in terms of performance condition have been identified as contributors to degradation , e.g. temperature, humidity, potential cycling, reactant gas composition; however, understanding the underlying mechanism associated with the structural composition is still facing significant challenge due to the intrinsic and complex multi-scale structure of CL [8].

## 1.4 CL fabrication – the formation of the microstructure

Limited Pt utilization and durability hinge on the microstructure of CL; therefore, it would be fruitful to look into the CL fabrication, through which the microstructure is formed. The standard procedure of CL fabrication involves several steps, including ink composition, ink preparation, and the fabrication process (deposition and drying of the catalyst ink), each of which has significant impact on the final microstructure (Fig. 1.7).

```
┌──────────────────┐      ┌────────────────────────────────────┐
│ Ink Composition  │◄─────│  E.g. Nafion, catalyst, solvent    │
└──────────────────┘      └────────────────────────────────────┘
        │
        ▼
┌──────────────────┐      ┌──────────────┐        ┌──────────────┐
│ Ink Preparation  │      │  Spraying    │────────│   Blading    │
└──────────────────┘      └──────────────┘        └──────────────┘
        │                 ┌──────────────┐        ┌──────────────┐
        │                 │  Ink-jetting │────────│   Brushing   │
        │                 └──────────────┘        └──────────────┘
        ▼
┌──────────────────┐      ┌──────────────┐
│Fabrication Process│◄────│ Ink Deposition│◄──────────┐
└──────────────────┘      └──────────────┘        ┌──────────────┐
        │                                          │   T, P, RH   │
        │                                          └──────────────┘
        │                 ┌──────────────┐        ┌──────────────┐
        │                 │Solvent Drying│◄───────│  Substrate   │
        ▼                 └──────────────┘        └──────────────┘
┌──────────────────┐                              ┌──────────────┐
│  Final Micro-    │                              │  Solution    │
│   structure      │                              │  Property    │
└──────────────────┘                              └──────────────┘
```
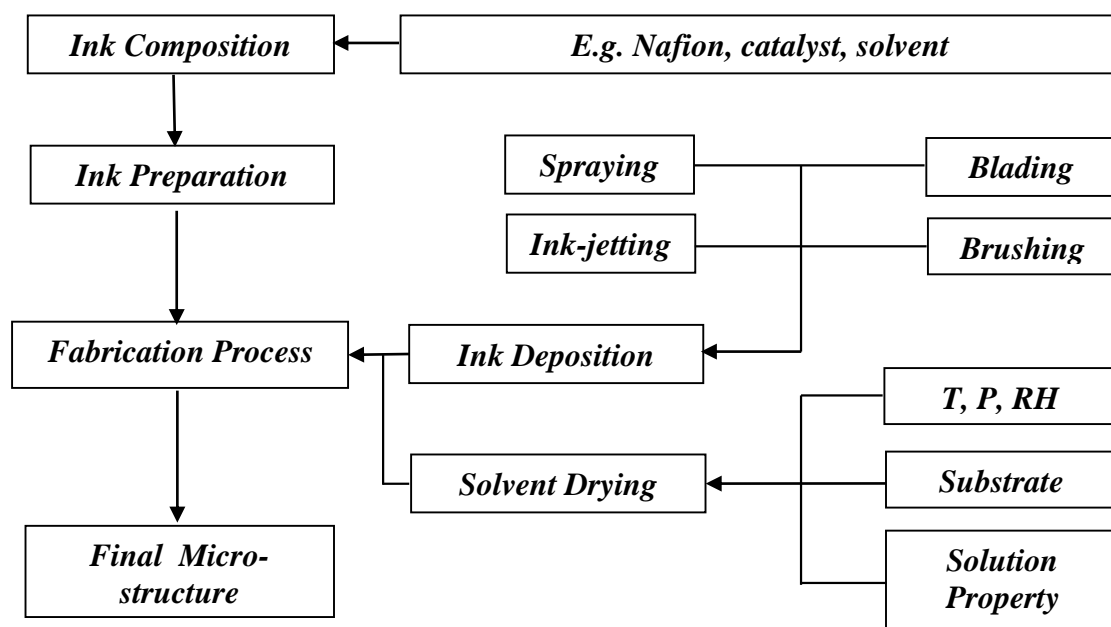
Fig 1.7. Schematic of CL fabrication. *T* represents temperature, *P* represents pressure, *RH* represents the relative humidity, of the drying environment, respectively.

The series of procedure can be further illustrated in Fig. 1.8. Through catalyst ink preparation, e.g. ultrasonic treatment, the mixture come into a fully mixed ink slurry composed of heterogeneous C/Pt aggregates dispersed within the solvent. Then in fabrication process, the catalyst slurry is applied onto a substrate and exposed to a solvent evaporative condition, C/Pt aggregates deposit to form heterogeneous porous microstructure as the solvent evaporates. As shown in Fig. 1.7, the primary CL fabrication technique that is low cost with high volume capability includes doctor-blading, brushing, spraying, ink-jetting and many others [13], which

7

will be reviewed in the next chapter. Those techniques, which are differentiated in terms of ink composition, ink preparation, and fabrication process, are all aiming to improve the catalyst utilization; however, the actual catalyst utilization often fail to achieve the target, e.g. a study shows that the upper utilization of platinum can be only around 50% [14], due to the complexities involved during the series of process, especially the solvent drying [5].
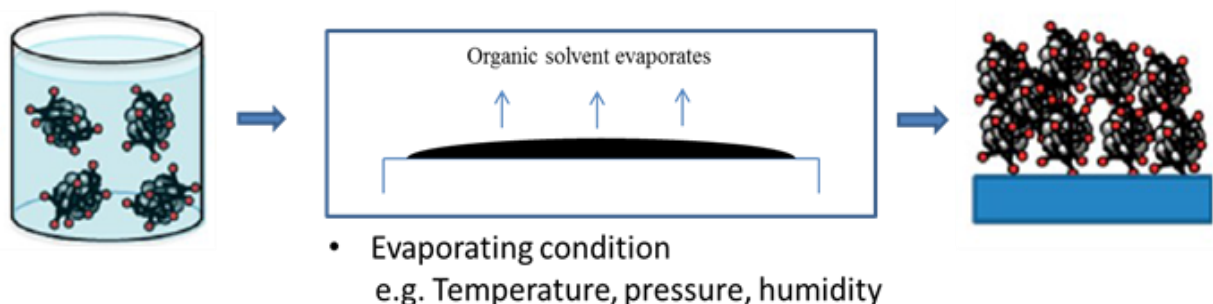


Fig 1.8. Schematic of the procedure of CL fabrication. It is normally composed of steps: ink preparation, deposition, and drying before forming into the final structure [5].

## 1.5 Motivation of the work

Central to various CL fabrication methods mentioned above, is the drying of catalyst ink solution spread on a substrate surface in the form of sessile drops or large thin films. As the catalyst ink is drying out shown in Fig. 1.8, drying condition (e.g. T, P, and RH), substrate (depends on specific fabrication technique), and physicochemical properties of the catalyst ink (depends on the ink composition and preparation) collaboratively determine the internal flow, and thus the particle transport and deposition. Some studies emphasized that the CL microstructure is significantly influenced by the drying process of the catalyst ink as solvent evaporates [39, 40, 41], therefore understanding the effect of drying dynamics of catalyst ink on the microstructure formation is of fundamental significance to improve the CL fabrication technique and thus increase the catalyst utilization.

## 1.6 Objectives and outline of the thesis

The objective of this study is to improve the fundamental understanding of the effect of drying dynamics on the microstructural formation during catalyst ink drying. It has been shown that there are significant commonalities in terms of the drying physics between a sessile drop drying (say, 10 μl) or a large colloidal film drying (say, 100 $m^2$) on an substrate surface [18], the present study will hence focus on the drying dynamics of catalyst ink drops. In this study, the characteristics of the microstructure of CL, as well as its formation from catalyst ink drop drying are experimentally examined.

The thesis is organized as follows. In Chapter 2, literature regarding the various CL fabrication techniques, with a focus on their ink composition and fabrication process, will be reviewed first; secondly, the effect of Nafion loading on CL performance by changing the weight ratio of ionomer and C/Pt will be reviewed. Finally, colloidal drop drying will be reviewed in details. Chapter 3 presents the experimental setup. Chapter 4 illustrates some key elements of colloidal drop drying to provide an overview of how drop drying will determine the final deposition. Chapter 5 presents the results and discussion, and finally, Chapter 6 presents the conclusions and recommendations out of the present study.

# Chapter 2 Literature Review

2.1 CL fabrication techniques and their developments

So as to increase the catalyst utilization and thus performance of CL, attentions need to be drawn to the microstructure formation of CL. The final microstructure and resultant performance of CL vary according to different CL fabrication procedures, e.g. material option and ink composition, ink preparation, dispensing methods, and casting procedure, as well as many others factors [13]. The first generation CL of PEMFC, which can be traced back to 1967, is using PTFE-bounded Pt black catalysts slurry to apply on the membrane to form the active layer [19][20]. This method exhibits excellent performance, however, is abandoned by its high cost, which is typically up to 4 mg Pt/cm$^2$.

2.1.1 The second generation CL (thin-film CL)

First invented by Ticinelli et al., the commencement of the second generation CL is to use carbon supported platinum particles (C/Pt) to replace the Pt black particles, and to mix with PTFE as solvent [22]. Later on, appropriate amount of Nafion is impregnated within the PTFE-bound CL to increase the ionic conductivity, and significantly decrease the platinum loading to 0.4 mg/cm$^2$ [23]. The thickness of the second generation CL is thinner than 20 μm, which significantly reduces the mass transport losses and thus increases the overall performance, so is also called the thin-film CL. The thin-film has been adopted as the industrial procedures for CL fabrication for the past three decades; in the following, the developments for the thin-film CL fabrication will be reviewed in details in terms of the ink preparation, dispensing methods, and the catalyst ink drying.

The PTFE-bounded CL is completely replaced by the Nafion-bounded thin film methods, which is first proposed by Wilson et al. [24]. In this method, the ink is prepared by mixing C/Pt, water,

Nafion solution, glycerol as the dispensing solvent, then cast onto the membrane directly; the ionic conductivity of the CL is greatly improved and with a platinum loading of 0.12-0.16 mg/cm$^2$ (less than 0.35 mg/cm$^2$) by employing hydrophilic Nafion as the binding materials. Normally, the casting procedure of directly applying the catalyst ink onto membrane is called CCM (catalyst-coated membrane).

The CL can be also cast onto PTFE blank (CCS, catalyst-coated substrate), then transferred to the membrane, which eases the fabrication and is usually employed in laboratory research [25]; or applied to the gas diffusion layer (CCG, catalyst-coated GDL) [39–41]. It should be noted that CCM method offers the highest performance by better ionic contact between the CL and membrane, and the thickness of CL fabricated by CCS (usually ~ 20 µm) is thicker than CCM, while the thickness of CL by CCM can be achieved very thin (< 10 µm); however, the benefit of CCM is obstructed by the drawback inherited in the coating process that the membrane would swell and deform as absorbing the solvent within the catalyst ink (e.g. solvent, water). Many researchers have been working on the optimization of the CCM to minimize this limitation, which renders CCM now the most industrially adopted MEA fabrication method [46, 47]. The thin film MEA manufacturing techniques have been continuously improved over these decades and are the most industrially adopted CL fabrication method.

Based on the ink composition proposed by Wilson et al. [24], iso-propanol is employed as the dispersing solvent instead of using glycerol; the CL is dried first under room temperature, then under 80 °C as a final step, which significantly simplifies the annealing procedures [25]. In [30], water is used as the dispersing solvent to simplify the process as well.

By fixing the C/Pt content, changing the Nafion content, Song et al. [27] found that the current density at a fixed output voltage can achieve an maximum value when the weight ratio of C/Pt to

Nafion (dry) is 3:1, which later on becomes the industrially adopted composition for the CL fabrication. Besides working on the ink composition, increasing the porosity in the CL by adding in pore former is also studied [31]. In order to prevent the Nafion decaying during operation, the Nafion is converted into thermoplastic form with large hydrophobic counter ions by adding Alkaline solution [27, 28], [31–33].

Though being widely used and successfully having decreased the Pt loadings (0.13 − 0.35 mg/cm$^2$), Wilson's method usually involves too many steps, whose complexities incur additional production cost. Uchida et al. proposed an ideal structure for electrochemical reaction and simplified preparation method, then first studied and demonstrated the importance of the microstructure and reactant gas network in the CL [34, 35].

In order to achieve uniformity of Nafion polymer on C/Pt particles, Uchida et al. proposed a new and simplified preparation method that Nafion solution is first mixed with organic solvent, and then the C/Pt particles are added in, then the mixture is transformed into a solution through ultrasonic treatment [34]. The state of the solution changes as the dielectric constant of the organic solvent changes: i) a precipitation is formed as $\varepsilon < 3$; ii) a colloidal suspension is formed as $3 < \varepsilon < 10$; iii) a solution is formed as $\varepsilon > 10$.

Later on, by mixing C/Pt and organic solvent first, then adding the Nafion solution, Uchida et al. found that the Nafion polymer coagulation is suppressed and the reaction area increased, and thus the Pt loading is decreased to 0.1 mg/cm$^2$ [35]. The CCG was employed for MEA in their experiments, the ink pastes are uniformly spread over carbon paper as GDL, and electrodes were hot-pressed on to Nafion membrane.

Then Shin et al. sprayed the catalyst ink onto GDL by air-brushing spraying technique, found that the Nafion polymer colloidal method generates nearly 20% improvement in the

electrochemical performance than the Nafion polymer solution method [36]. The improvement is primarily attributed to the appropriately increased porosity, and accordingly increased ionic conductivity and enhanced mass transfer for reactant gas.

One of the biggest differences which differentiate the spraying method from doctor blade, screen-printing, rolling, and brushing is the solid content of the catalyst ink. The solid content (Nafion and C/Pt particles) usually needs to be lower than 2 wt % to avoid nozzle-clog, while the solid content is usually higher than 5 wt % in other casting methods. Spraying including some advanced versions, e.g. ultrasonic spraying [44], electro-spraying [45], efficiently mitigate the membrane swelling and deforming problem, and significantly increases the catalyst utilization; however, the high production cost primarily due to the equipment cost results in the main impedance for its large scale commercialization.

Yang et al. employed five different solvents, includes butyl acetate ($\varepsilon = 5.01$), iso-amyl alcohol ($\varepsilon = 15.8$), diethyl oxalate ($\varepsilon = 8.10$), ethylene glycol ($\varepsilon = 38.66$), and ethylene glycol dimethyl ether ($\varepsilon = 5.5$), and CCS method. They found that ethylene glycol showed a best performance than other solvents, but fails to provide qualitative explanations for the differences in performance [37].

Fernandez et al. studied the effect of the evaporation rate and solvent composition on the catalytic layer microstructure using CCG method, found that the MEA performance might be collaboratively dependent on dielectric constant ($\varepsilon$), viscosity ($\mu$), and boiling point (t). The CL prepared by the solvent with lowest dielectric constant shows the highest performance, and the increased evaporation rate effectively reduces the contact resistance between CL and GDL and improves the solute distribution [38].

Therdthianwong et al. employed seven different solvents and CCM method, including iso-propanol ($\varepsilon$ = 18.3, $\mu$ = 2.1 cP, t = 82°C), ethanol ($\varepsilon$ = 24.3, $\mu$ = 1.07 cP, t = 78°C), acetone ($\varepsilon$ = 20.7, $\mu$ = 0.31 cP, t = 56 °C), deionized water ($\varepsilon$ = 80.4, $\mu$ = 0.89 cP, t = 100°C), ethylene glycol ($\varepsilon$ = 37, $\mu$ = 16.1 cP, t = 197.3 °C), EGDME ($\varepsilon$ = 7.2, $\mu$ = 0.46 cP, t = 85 °C), EGDEE ($\varepsilon$ = 3.8, $\mu$ = 0.7 cP, t = 121.4 °C), and found that iso-propanol provided the highest cell performance [39]. Based on the conformity of their results to Yang et al. and contradiction to Fernandz et al., they concluded that for CCM or CCS method, CL prepared by solution methods shows better performance, for the solutes penetrate into membrane, which reduces the resistance between the CL and membrane; vice versa, colloidal method is of a better option for CCG method, for colloids with larger sizes suspending (up to around μm) do not easily filtrate through the permeable substrate.

By employing six different solvents with varying dielectric constants, Huang et al. conducted a comprehensive study on the effects of dispersion solvents on final structure of CL and resultant performance of MEA. They found that the final morphology of catalyst deposition varies significantly as the solvents change, even in some cases cracks are incurred and adversely affect the catalyst utilization [40]. In addition, the effect of temperature during the catalyst ink drying on the morphology of catalyst layer is also significant. Park et al. found that increasing the annealing temperature to facilitate the solvent evaporation, and enlarges the pore volume specifically in secondary pores, and then increases the I-V performance [41]. Liang et al. successfully modified the CCS method by improving the technique involved in this process, e.g., adjusting the viscosity of solution by altering the composition of the solvent, drying the catalyst layer at different temperature [42].

2.1.2 Third generation CL (ultra-thin CL)

In order to increase the utilization of electro-catalyst, it was found that instead of employing carbon-supported catalyst particles, direct deposition of platinum onto the electron conductor (gas diffusion layer) with ionic conductor (Nafion polymer) partially covered offers proton a much easier accessibility to catalyst site, which is similar to the first generation CL fabrication. Based on this idea, sputtering deposition [46-50], pulse laser-deposition [51, 52], ion-beam [53, 54], electro-deposition methods [55–59] has been developed to achieve MEA with ultra-thin CL (~ 1 μm), and significantly reduced the platinum loading (~ 0.1 mg/cm$^2$ or ever lower), e.g. O Hayre et al. reported that by using sputtering deposition methods, they made MEA with an ultra-low Pt loading of about 0.04 mg/cm$^2$ and generate a maximum power output up to three-fifths that of a commercial E-TEK MEA [49].

For the third generation CL fabrication, inkjet printing (IJP) needs to be specifically highlighted for its features, e.g. drop-on-demand, uniform jetting, and patterning capability [60-63]. The basic idea of IJP is to apply discrete drops, usually with volume of several pico-liter, onto a certain substrate to fashion a designed pattern, which differentiate from other third generation techniques. The platinum loading employed by IJP can be as low as 0.05 mg/cm$^2$, and with thickness < 2 μm, yet has a performance which is comparative to the CL of 0.4 mg/cm$^2$ fabricated by traditional thin-film methods [62]. Though the ultrathin CL including IJP significantly increases the catalyst utilization by avoiding C/Pt agglomerate, it is still in the laboratory stage and not being considered as economically viable alternative to thin-film fabrication due to its high cost for scaling up, and water-flooding issue.

## 2.2 Effect of Nafion loading on performance

It has been indicated through experiments that Nafion loading has a significant impact on the microstructure and performance of CL [24][64]. Since Song et al. [27] proposed that optimal

15

weight ratio of Nafion to C/Pt is 1:3 without considering the platinum ratio on Carbon, many researchers studied the optimal ratio of Nafion to C/Pt with various platinum weight ratio on C/Pt and its influence on the microstructure [26, 63–70]. Passalacqua et al. defined a parameter NFP (Nafion percentage), $NFP = L_{Naf} / (L_{Naf} + L_{Pt} + L_C)$, to quantify the Nafion loading, where $L_{Naf}$, $L_{Pt}$ and $L_C$ represent the loading of Nafion, Platinum and carbon in mg/cm$^2$, respectively [68]. The Nafion loading corresponding to the maximum performance is referred as optimum NFP. The optimal ratio of Nafion to carbon falls in the range of 0.7-1.0 in general [64], but optimal *NFP* is determined by the platinum loading and fabrication technique as well. In our study, we only reviewed those studies using 20% C/Pt (weight ratio of platinum accounts for 20% of C/Pt), which is the most commonly used C/Pt type. Experimental studies using various Nafion loading are summarized in Table 1.

Table 1 Comparison of different optimal NFP reported in literatures

| References | Deposition method | Pt loading mg cm$^{-2}$ | Optimum NFP |
|---|---|---|---|
| Wilson et al. [24] | CCM, thin film | Various loading | 25-28% |
| Poltarzewski et al. [65] | CCL, thin film | 0.5 | 23% |
| Antolini et al. [67] | CCL, brushing | 0.2 | 40% |
| Passalacqua et al. [68] | CCL, thin film | 0.1 | 33% |
| S.J. Lee et al. [23] | CCM, proprietary rolling technique | 0.4 | 50% |
| Qi and Kaufman [28] | CCL, spraying | 0.2 | 30% |
| Gode et al. [69] | CCM, spraying | 0.1 | 41% |
| Chaparro et al.[14] | CCM, electrospray | 0.17 | 15.5% |
| Sasikumar et al. [70] | CCL, spraying | 0.1/0.25/0.5 | 51%/41%/20.5% |
| Shukla et al. [61] | CCM, ink-jetting | 0.05 | 40% |

Note that the deposition method varies between doctor-blading, brushing, spraying, as well as other thin-film techniques. In many of the literatures in Table 1, the specific technique was usually not mentioned.

The optimum NFP varies in a wide range from 15.5% to 50% as the platinum loading and deposition methods change. All of those studies in Table 1 employed an ex-situ approach which directly draws linkage between the performance and various factors evolved in fabrication

process, e.g. drying condition, ink composition, and deposition methods, and did not look into the microstructure formation through the solvent drying [14, 23, 29, 61, 66-71].

2.3 Colloidal drop drying

For those industrially viable CL fabrication techniques, the solvent drying process of thin film method, e.g. doctor-blading and brushing, can be regarded as an extended drop drying, and the solvent drying process of spray and ink-jetting can be regarded as impinning and drying of multiple drops, therefore the catalyst ink drop drying is an excellent starting point to understand the physical complexities in practical CL fabrication [18]. Although a good body of studies are available for the drying of colloidal drops with nonvolatile solutes due to its importance in a variety of practical applications, such as printing, coating and manufacturing of self-assembled novel structured materials [72], few studies have been devoted to the drying process of catalyst ink drops.

Deegan et al. performed pioneering studies on the formation of ring-like stains, and the accumulation of particles at the periphery of the deposits, commonly referred to as "coffee-ring" phenomenon, when liquid drop containing dispersed solid particles evaporates on a substrate surface [73–75]. Through both experiment and analysis based on lubrication theory incorporating Maxwell approach for the pure sessile drop drying [76], they showed that the migration and concentration of solid particles leading to the coffee-ring is due to a radially outward flow in the drop driven by the highest solvent evaporation at, hence carrying the particles to, the pinned contact line.

Hu and Larson, in a series of studies [77-80], found that the non-uniform evaporation over the drop surface induces a temperature gradient that produces a surface-tension gradient on the free surface which would drive the solvent to flow radially inward. The radially inward flow, which

is also termed as thermal Manragoni flow, leads to a circulation flow inside the drop when coupled with the radially outward flow (the evaporation-driven flow) shown by Deegan et al. Therefore, depending on the strength of the thermal Manragoni flow, the solid particles can concentrate either at the contact line forming the ring-like structure, or at the center of the drop where the stagnation point of the flow exists. The coffee-ring phenomenon occurs when the thermal Marangoni flow is negligible. Ristenpart et al. found that the direction of thermal Marangoni flow is actually controlled by the contact angle and the ratio of the substrate to liquid thermal conductivities for evaporating sessile drops on a substrate surface [81]. Bhardwaj et al. conducted a numerical simulation involving full Navier-Stokes fluid, heat and mass transport equations incorporating the receding of the contact line [82], and confirmed the direction of the thermal Marangoni flow as found in Ristenpart et al., and the impact of the thermal Marangoni flow on the final deposition of the solid particles as pointed out in Hu and Larson's studies. A further study considered the interaction between the solute and substrate, in addition to the evaporation -driven flow and the thermal Marangoni flow, and the competition among these three flow effects leads to a variety of complex deposit structures [83].

Nikolov and Wasan investigated experimentally the mechanism driving particles to form organized deposit structures during drop evaporation at the pinned contact line for small contact angles [84]. It is shown that particles are driven into the wedge region near the contact line by the thermal Marangoni flow for small wedge angles with a pinned contact line, and the particle deposit structure is self-organized in the confines of the wedge surfaces due to the stagnation point flow, rather than the capillary attraction arising from the menisci formed between the particles. Further, the importance of the surfactant-induced solutal Marangoni flow is demonstrated by adding small amounts of surfactant. The effect and strength of thermal

18

Marangoni flow was studied by Zhang, et al. on the deposit formation for colloidal drops drying on heated substrate [85].

Most of the studies described above were focused on the deposit pattern formation for the drying of drops made of the solvent-particle binary mixtures; however, the complexities of the deposit structure could arise from the surfactant-doped triple mixtures. A systematic investigation was carried out experimentally by Morales et al. regarding the effect of nonionic surfactant on evaporating drops, the contact line behavior and the dried deposit formation are significantly affected by the presence and the concentration of the surfactant [86]. Still et al. used ionic surfactants for the colloidal drops, and observed a qualitatively different drying dynamics [87]. Specifically they noticed that a strong Marangoni flow towards the center of the drop, created by the ionic surfactants, results in Marangoni eddies that prevent most of the spheres from reaching the contact line, hence more uniform deposit formation, particularly near the periphery of the drops. Senses et al. investigated the effect of polymer in a particle-lad solution on the drop drying dynamics and the deposit formation [88]. They showed that the phase separation of colloids and polymers leads to stripe formation near the contact line, and the polymer concentration influences the dried deposit structure via a combined mechanism of the phase separation and the Marangoni flow.

As it is clear from the above, the dried deposit formation from colloidal suspension drops is mainly determined by the strength of Marangoni flow driven by surface tension gradients. Surface tension gradients can be produced by the non-uniform temperature distribution over the drop surface, whether through the non-uniform evaporation or through heating/cooling the substrate surface, or by doping the drop solution with surfactants or polymers. These previous studies are mainly based on the monodisperse spherical particles in the solution. However,

particle size distribution, particle shape, and the wettability of the solution-substrate surface all have significant impact on the contact line drying dynamics and final depositions patterns. For example, observations have been made for finger ring deposition at the drop periphery with bi-dispersed colloidal solution [89], uniform deposition by using ellipsoidal-shaped colloidal solution [90], a variety of deposition patterns with different substrate surface wettability characteristics [91]. Crivoi and Duan recently carried out a Monte Carlo simulation to investigate the factors involved in the deposit formation during the drying process of pinned sessile colloidal drops [92].

As mentioned earlier, a catalyst ink used for the fabrication of the catalyst layers in PEM fuel cells involves platinum nanoparticles on carbon mesoparticles (C/Pt), Nafion polymer (ionomer), chemical solvent and water, it is therefore a quadruple colloidal system with polydisperse particles having highly complex physico-chemical properties [5]. The catalyst ink is typically ultrasonicated to disperse the particles in the solution. During the ultrasound treatment, C/Pt particles coalesce into C/Pt agglomerates; bridging force due to the ionomer entanglement leads to cross-linkage among C/Pt agglomerates, which produces a wide range of sizes of C/Pt agglomerates, from hundreds of nm to several μm [37]. As a result, the drying process of catalyst ink drops on a substrate surface is expected to be quite involved with few studies available in literature, and only found in work done by Tembely et al., in which they still applied lubrication theory on the simplified Binary-Mixture Drop, without considering the polymer and hetero-dispersion effect, to numerically study the deposition profile of catalyst ink drop evaporation [93].

# Chapter 3 Experimental Setup

In this study, the characteristics of the microstructure of CL, as well as its formation from catalyst ink drop drying are experimentally examined. The real-time drying dynamics are observed with optical microscopy to understand the microstructure formation. The experimental setup consists of two major components: first, catalyst ink preparation and deposition; second, drying dynamics and dried pattern acquisition. Figure 3.1 shows the schematic of the drop deposition and its drying dynamics acquisition. The experiments are carried out typically in laboratory room conditions (the temperature is around 21.6º C and humidity is 70 %).
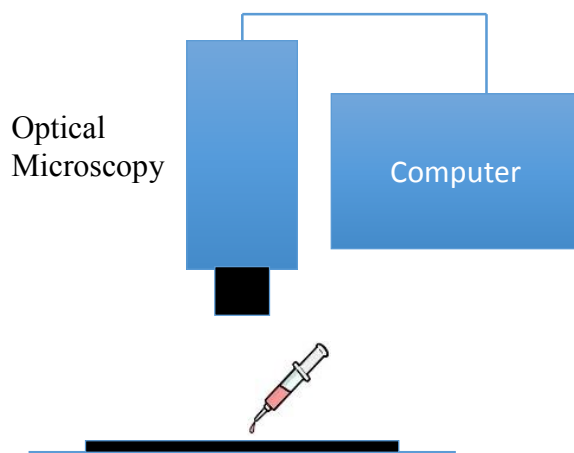


Fig 3.1. Schematic of the drop deposition and its drying dynamics acquisition

## 3.1 Catalyst ink preparation and deposition

**The options for ink composition and materials.** The catalyst ink is prepared by mixing C/Pt particles (HP 20% Platinum on Vulcan XC-72) and 5% wt Nafion solution (Ion Power D520, 45±3% for water, 50±3% isopropyl alcohol, 5% Nafion®PFSA ionomer), and isopropyl alcohol. Catalyst ink samples are prepared using various Nafion loadings while the C/Pt loading is held constant that $W_{Nafion}/W_{Nafion+Pt}$ ranges from 6.25 % to 62.5 %, covering the range of ratio found in literatures. The solid content (C/Pt particles and Nafion polymer) is maintained at ~ 0.8 wt% in the solution. The low solid content (usually is lower than 2wt% for spraying) used in this

study is to ensure that the light can go through the drop and thus the drying dynamics can be recorded by optical microscope.

**Catalyst ink preparation.** Figure 3.2 shows all the equipments used for the catalyst ink preparation. In our sample, the 4 ml vial is used to contain the ink (Fig. 3.2 (a)). The C/Pt particles is weighed by a balance (Sartorius Practum 224-1S, weighing capacity of 220 grams with resolution to ± 0.1 mg, Fig. 3.2 (b)), then put into the vial. Organic solvent is added into the vial using pipette (Eppendorf Research Plux, capacity of 1 ml with resolution to ± 1 μL, Fig. 3.2 (c)), then the mixture needs ultrasonic treatment (Fisher Scientific 5510DTH, Fig. 3.2 (d)) for 10 − 15 minutes to disperse the C/Pt particles. Finally, Nafion solution is added in using pipette (Eppendorf Research Plux, capacity of 20 ul with resolution to ± 0.1 μL), the ink solution is subject to 90 min of sonication to ensure the colloidal suspensions are uniformly dispersed in the solution. The procedure for ink preparation above follows the Nafion polymer colloidal method invented by Uchida et al. [35].

**Catalyst ink drop deposition.** Drops of catalyst ink with volume ~ 1 μL are dispensed by syringe (Hamilton 7001 KH SYR, capacity of 1 μL with resolution to ± 0.01 μL, Fig 3.2. (e)) onto new microscopy slides without any pre-treatment (Fisher scientific microscopy slide, Fig. 3.2 (f)). The microscopy slides must be levelled horizontally before drop deposition.

3.2 Drying dynamics and dried pattern acquisition

Figure 3.3 shows the Carl Zeiss optical Microscope, Axio Zoom V16 (magnification ranges from 0.7x to 26x, 1040 pixels * 1388pixels, 14 fps) used for capturing the real-time dynamics during the drop evaporation from either backlighting (light goes up from the bottom of the sample holder) or front lighting (vice versa). Backlighting provides better contrast for the image (Fig. 3.4 (a)); while front lighting might create shadow if the light is not projected correctly upon the

22

sample when the field of view is large (Fig. 3.4 (b)), but it can capture interferometry patterns of the free surface on the evaporating droplets via reflected light when focusing on a point (Fig. 3.4 (c)). The lighting uses LED as the light source which emits cold light and does not affect the solvent evaporation. Note that if not being specified, the image is acquired using backlighting in the following.

Additional equipment for the catalyst ink properties measurement includes: the surface tension of the catalyst ink is measured by Dataphysics DCAT 11 (measuring capacity of 1000 mN/m, and resolution of ± 0.01 mN/m, Fig. 3.5 (a)); the side view drying profile is recorded by ramé-hart 100-25-A Goniometer (Fig. 3.5 (b)).



(a)                                         (b)                                         (c)

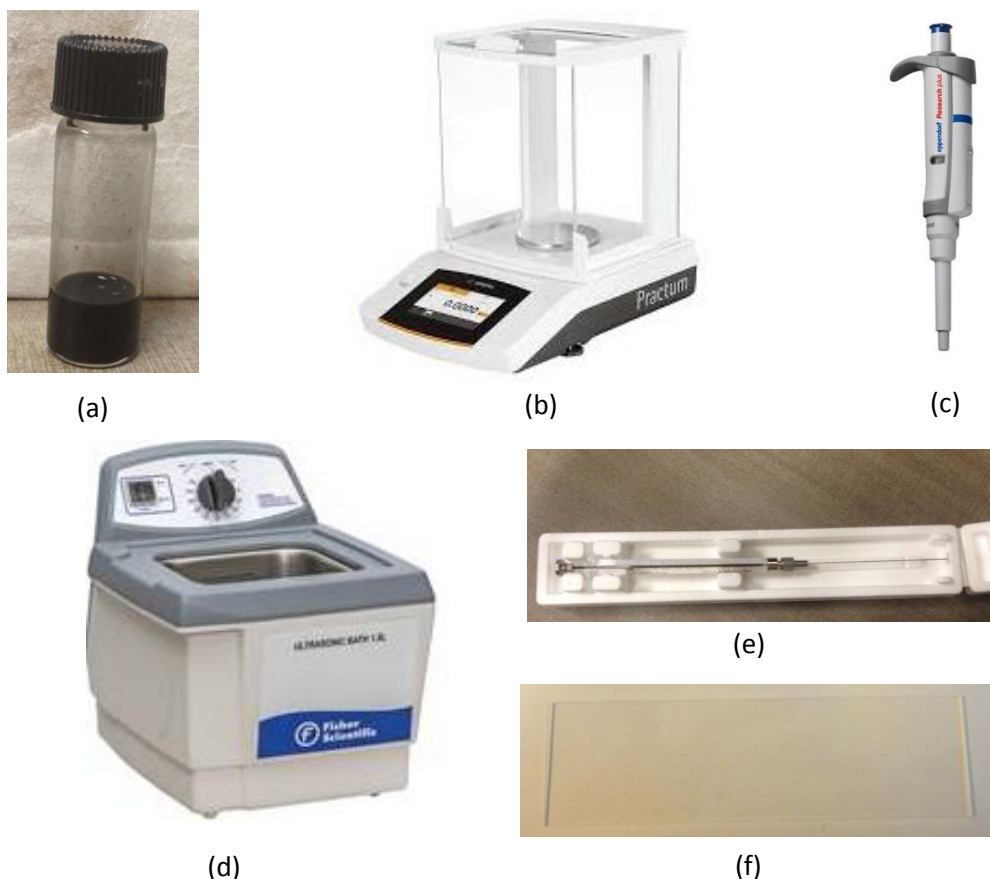(d)                                         (f)

Fig 3.2. Experimental facilities used for catalyst ink preparation and deposition. (a) Sartorius Practum 224-1S, weighing capacity of 220 grams with resolution to ± 0.1 mg. (b)  Eppendorf Research Plux, capacity of 1 ml with resolution to ± 1 μL. (c) Eppendorf Research Plux, capacity of 1 ml with resolution to ± 1 μL. (d) Fisher Scientific 5510DTH. (e) Hamilton 7001 KH SYR, capacity of 1 μL with resolution to ± 0.01 μL.
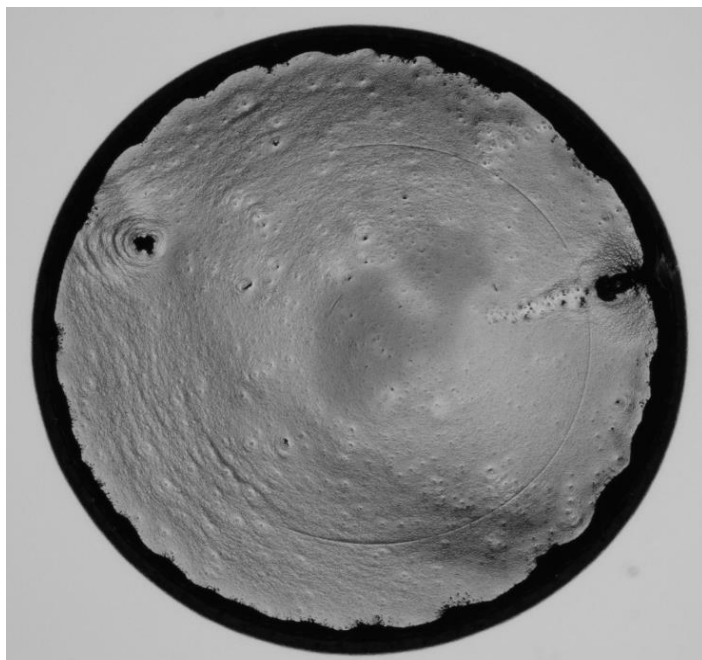
Fig 3.3 Carl Zeiss optical Microscope, Axio Zoom V16
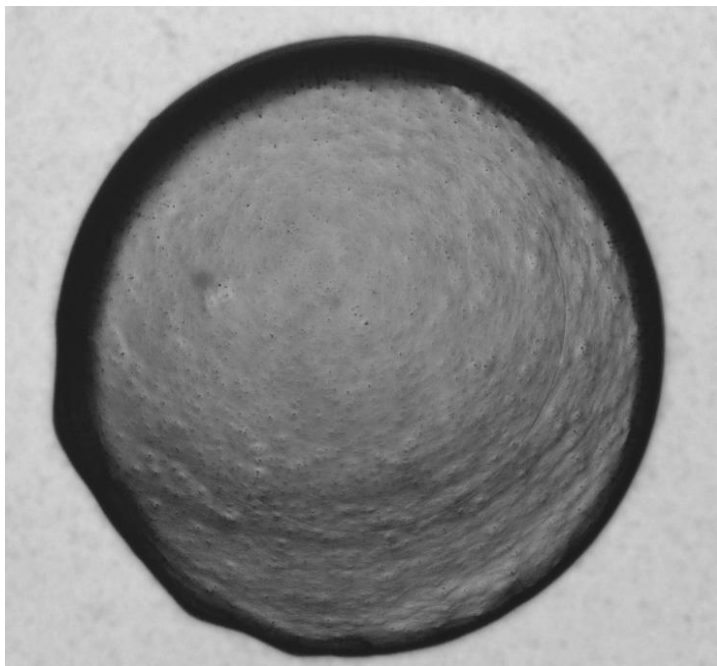


Fig 3.4 (a) Whole drop using

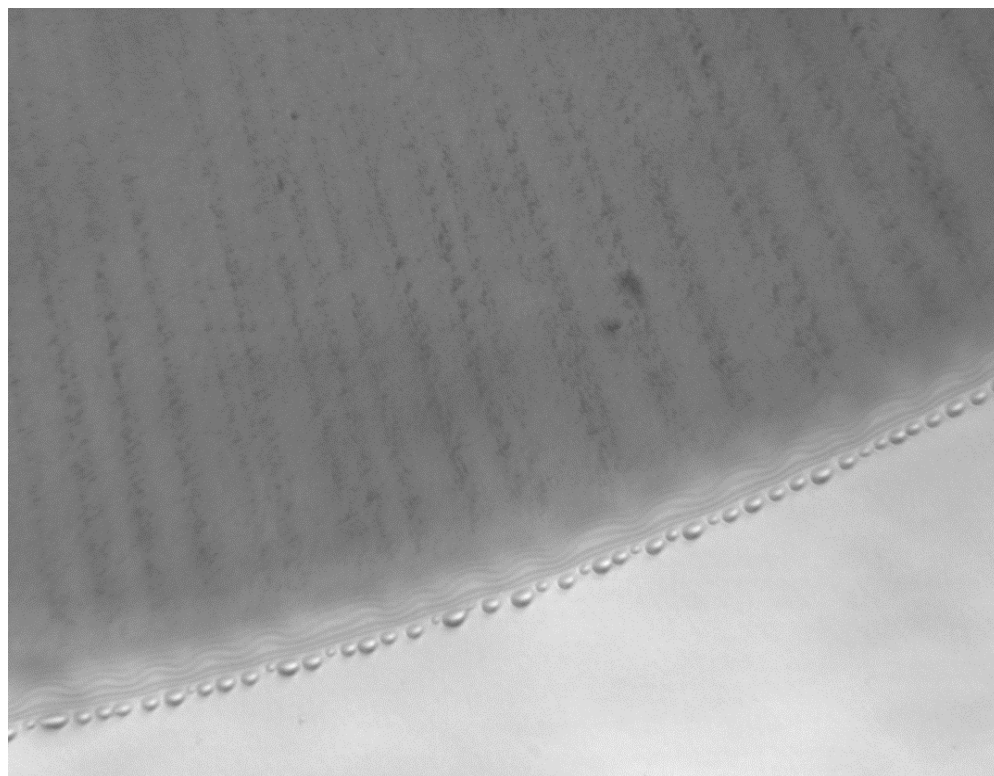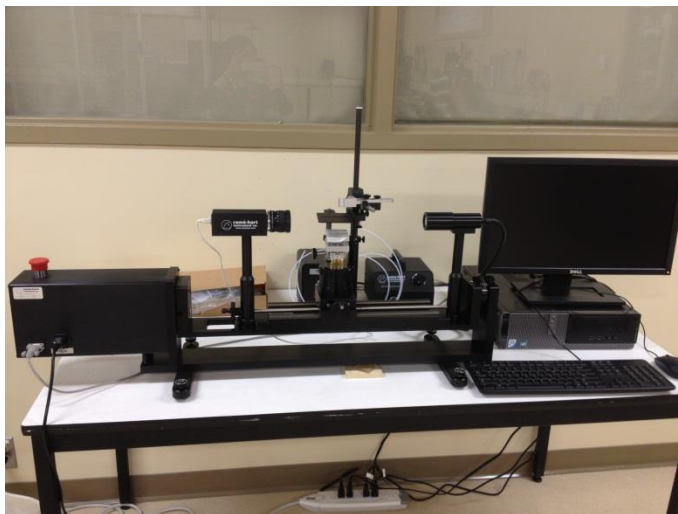Fig 3.4 (b) Whole drop using front lighting



Fig 3.4 (c) Focusing on the edge using front lighting

Fig 3.4. Imaging of catalyst ink drop samples acquired using backlighting and front lighting. (a) Whole drop using backlighting. (b) Whole drop using front lighting. (c) Focusing on the edge using front lighting.

(a)

(b)

Fig 3.5. Experimental facilities for properties measurement of the catalyst ink. (a) Dataphysics DCAT 11 with measuring capacity of 1000 mN/m and resolution of ± 0.01 mN/m for surface tension measurement of the catalyst ink. (b) 100-25-A Goniometer for side view profile measurement.

# Chapter 4 Theoretical background of colloidal drop drying

The final deposition of the dried pattern varies as drying condition (e.g. T, P, and RH), surface properties of the substrate, and physicochemical properties of the colloidal drop change. These three factors would collaboratively dictate the complex transport phenomena occurring in the evaporating drop, thus its resultant particles deposition. As a colloidal drop are drying on a substrate, in most cases, the particles inside the drop are found to consolidate at the edge, leaving a coffee ring as the drop dries out shown in Fig. 4.1.



Fig 4.1. A coffee ring as a coffee drop dries out [94]

## 4.1 The origin of coffee-ring formation

When the drop is dispensed onto a substrate, its spread thins the fluid layer, and the contact line stops to advance when the flow towards the contact line in the bottom layer and the flow away from the contact line in the upper layer balance (Fig. 4.2). When the contact line pins, a wedge film with a slope toward the substrate forms. Over time, the volume of the drop diminishes as the drop evaporates. The evaporative flux of drop, $J$, increases from the apex down to the contact line, leading to a higher solvent loss at the edge than the center of the drop. In order to keep the contact line pinned, an outward convective flow is triggered to replenish the solvent loss at the

edge. The contact line pinning continues to accrue as more particles are brought under the outward convective flow and accumulate at the edge, and eventually becomes a coffee-ring as the drop dries out (Fig. 4.3).
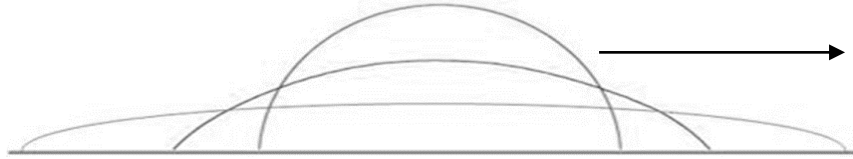


Fig 4.2. Contact line advances and pins after the drop is deposited onto a substrate
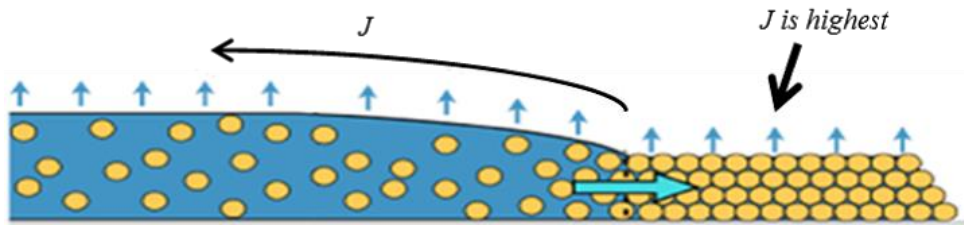


Fig 4.3. Schematic of the coffee-ring formation of the colloidal film or drop drying. $J$ is the evaporative flux [97].

## 4.2 The evaporative flux over the drop

Based on the assumption that the shape of the drop is spherical, Deegan established a quantitative expression of the mass evaporative flux variation over the drop, which is described in the form [73]:

$$\vec{(J} * \vec{n)} = J_0 (\Theta) (1 - \tilde{r}^2)^{-\xi(\Theta)}$$

where $J$ is the vapor mass flux at the liquid/air interface at distance of r away from the center of the drop, $\Theta$ is the contact angle and decreases with time. $J_0 (\Theta)$ is the evaporation flux at the center of the drop, $\xi(\Theta)$ is a fitting parameter denoting the non-uniformity of the evaporative flux over the drop and proposed as $\xi = (\pi - 2\Theta)/(2\pi - 2\Theta)$. And $\tilde{r} = r/R$, R is the contact-line radius. $\vec{n}$ is the unit vector normal to the surface.

28

From the equation above, it can be found that the evaporative flux over the drop depends on the contact angle and thus the shape of the drop as it sits on substrate. Later on, Hu et al. adopted this expression and used FEM analysis to correct the value for $\lambda$ that $\lambda = 0.5 - \Theta/\pi$, which was reported with higher precision [77]. Hu et al. also defined two stages for colloidal drop evaporation shown in Fig. 4.4. In the first stage, the contact angle pins and continues to decrease as the drop dries out (Fig. 4.4 (a)). As the contact angle decreases below a critical value, the drop drying enters into the second stage where the contact line starts to recede (Fig. 4.4 (b)). The contact angle for the transition between the two stages are collaboratively determined by the drying condition, the surface properties of the substrate, and the physicochemical properties of the colloidal drop.

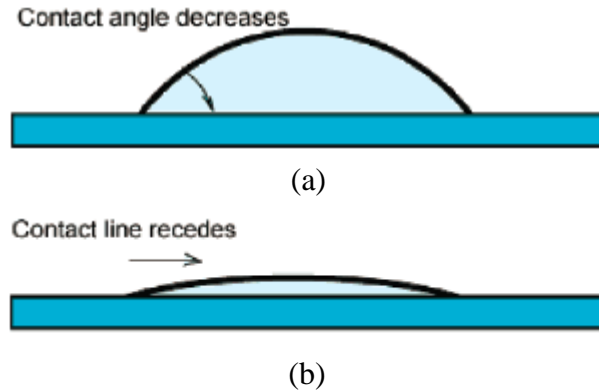Contact angle decreases

(a)

Contact line recedes

(b)

Fig 4.4. Schematic of the drop evaporation process drying in two stage: contact angle decreasing and contact line receding [78]. (a) Contact angle decreasing and (b) Contact line receding.

It should be noted that in actual situation the shape of a sessile drop does not always take on a spherical shape [95]. As the drying conditions are maintained, the shape of the sessile drop is determined by two aspects: the surface properties of the substrate and the properties of the solution. A simple but effective criterion is to use the capillary length, $K^{-1} = \sqrt{\sigma/\rho g}$, $\sigma$ is the surface tension of the liquid/air interface of the fluid, $\rho$ is the density of the fluid, g is the gravitational acceleration. When $R \ll K^{-1}$, where R is the radius of the drop, the capillary forces

dominates the gravity force, therefore the drop takes on the shape of spherical cap as its stops

pinning shown in Fig 4.5. (a). Vice versa if R » K$^{-1}$, the gravitational effect dominates. The drop
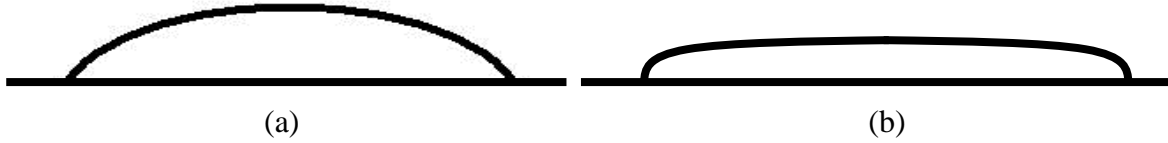
takes on the shape of puddle shown in Fig. 4.5 (b).



(a)                                                                     (b)

Fig 4.5. Shape of the sessile drop changes as surface tension of the liquid changes. (a)  R « K$^{-1}$; (b) R » K$^{-1}$.
R denotes the radius, K$^{-1}$ denotes the capillary length of the drop.

## 4.3 Circulation flow in evaporating drops

Circulation flows due to reversed flow opposite to the outward convective flow near the contact

line are usually incurred in evaporating drops and have significant impact on the final particle

deposition. The reversed flow is driven by surface tension gradient along the liquid-air interface.

Non-uniform evaporative flux over the drop would leads to temperature difference on the

surface, and further results in surface tension gradient. Accordingly, a tangential stress, $\tau$, is

triggered by the surface tension gradient, which can be represented as:

$$\tau = t * \nabla_s \gamma = \beta \, (t * \nabla_s T)$$

where t is the tangential unit vector, $\nabla$s is the surface gradient, $\gamma$ is the surface tension. $\beta \equiv \partial \gamma / \partial T$

is the material parameter and is negative for most liquids. In our case, $\beta$ is also negative for

isopropanol, therefore the stress decreases as the temperature increases on the free surface.

Ristenpart et al. experimentally and analytically proved that the circulation flow can either

radially flow outward along the substrate and then radially flow back inward along the air/liquid

interface, or vice versa [81]. Through their study, the circulation flow direction can be

determined by a qualitative criterion which is based on the coupling effect of the ratio of thermal

conductivity of substrate to liquid, and the contact angle,

$$k_R^{crit} = \tan(\theta_c)\cot(\frac{\theta_c}{2} + \frac{\theta_c^2}{\pi})$$

where $\theta_c$ is the contact angle, and $k_R$ is the ratio of the thermal conductivity of the substrate, $k_s$, to liquid, $k_l$, $k_R^{crit}$ is the critical value of $k_R$. This criterion can be applied to situations as $0 \le \theta_c \le \frac{\pi}{2}$. This relation between $k_R^{crit}$ and $\theta_c$ is depicted as the curve in Fig. 4.6, in which if $k_R > k_R^{crit}$, then the flow direction will follow the pattern above the curve, and vice versa.

This relation can be understood in a physical way. The evaporative flux is increasing from the apex to the edge, which indicates that more energy (heat) will be brought away due to evaporative cooling effect. $k_R \gg 1$ denotes that the substrate with much larger thermal conductivity compared to the drop serves as an energy reservoir to readily provide heat to the drying drop; therefore, temperature is the highest at the contact line and decreases as approaching to the apex of the drop. In contract, if the conductivy of the substrates is not sufficiently large, so that the heat is not provided readily to the drop, the temperature is lowestest at the contact line.
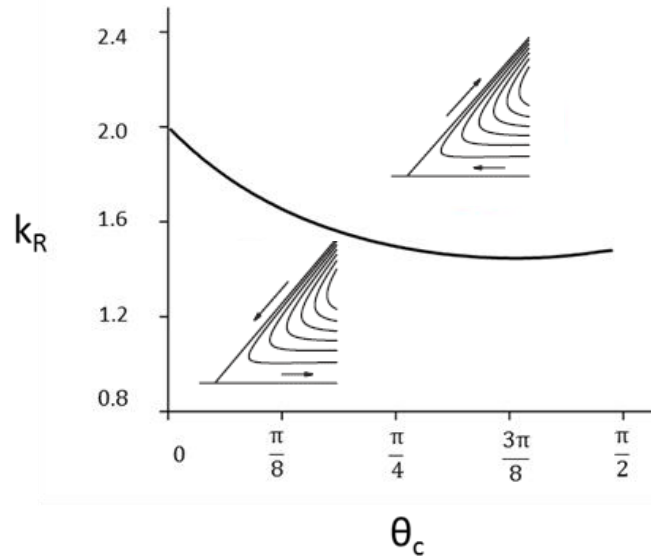


Fig 4.6. Dependence of the circulation direction of the thermal Marangoni flow inside evaporating drops on the contact angle and ratio of the thermal diffusivity of the substrate to the liquid. Regions above and below the line correspond to the circulation directions sketched in the respective streamlines [81].

31

# Chapter 5 Results and discussions

Evidence shows that besides being mixed with C/Pt particles to form C/Pt aggregates, Nafion is also aggregated by itself and dispersed in the catalyst ink. As the Nafion loading is varied, the physical-chemistry properties of the ink also changes [5]; accordingly in our study, it shows that the drying dynamics and resultant microstructure of the dried catalyst ink drops also vary significantly. In order to gain a decent understanding of the effect of the Nafion loading on the drying dynamics and dried microstructure formation, catalyst ink drops with three Nafion loadings by weight, $W_{Nafion}/W_{Nafion+C/Pt}$ = 6.25%, 25%, and 62.5% will be presented and investigated in the following. The drop dryings of the three Nafion loadings demonstrate representative drying patterns as the Nafion loading is continuously increased.

## 5.1 Pattern formation of $W_{Nafion}/W_{Nafion+C/Pt}$ = 25%

In this section, the drying and dried pattern characterization of catalyst ink drops with the ratio of Nafion to C/Pt is 1:3 by weight, which is considered to be the most common catalyst ink formulation in industrial CL fabrication [13], is presented. The volume of each drop is 1 μl ± 0.01 μl, and around 20 drops of each sample are deposited.

### 5.1.1 Dried pattern and its characterization

It is shown in Fig. 5.1 that the C/Pt aggregates accumulate and form a coffee-ring at the edge as the drop dries out. Figure 5.2 shows the microstructure of the rectangular region marked in Fig. 5.1. In Fig. 5.2 (a), it gives a clear overview of the non-uniformity of the dried pattern that the deposition is amassed at the edge comparing to the diluted deposition at the inner region. Figure 5.2 (b) shows that C/Pt aggregates deposit inside the drop in the form of curved slim leaves, most of which connect together to form into larger aggregates. At the coffee ring region, the light fails to go through the thick deposition, instead of using optical microscopy, the morphology of the

deposition is acquired with scanning electron microscope (SEM). From Fig. 5.2 (c), one can see that the microstructure of the dried coffee-ring layer is highly non-uniform, composed of large numbers of bumps and heterogeneous porous microstructure.
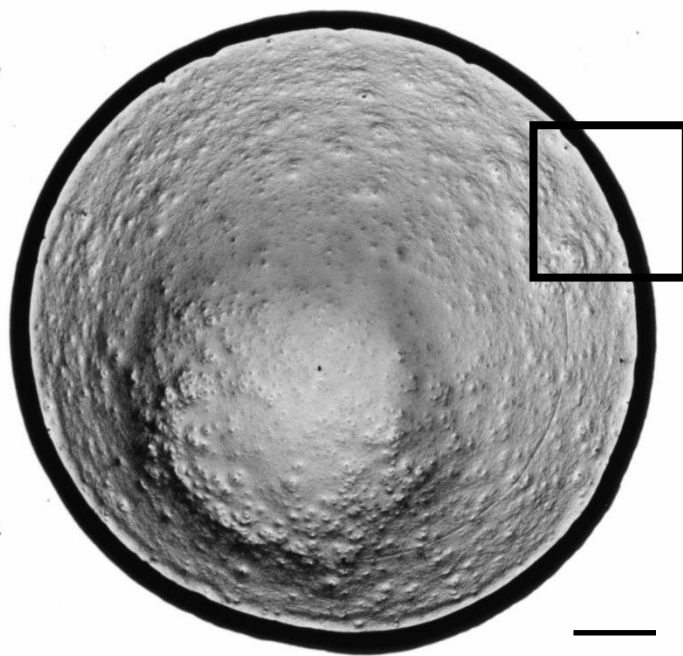


Fig 5.1. Dried pattern of the catalyst ink drop of $W_{Nafion}/W_{Nafion+C/Pt} = 25\%$ (1 μl). The scale denotes 500 μm.

The top view and side view SEM image of a freshly made catalyst layer using spraying technique are shown in Fig. 5.3 as compared to the microstructure of the drop coffee-ring made above. The catalyst layer was made using the same ink composition and following the standard procedure of CCM [34]. Comparing Fig. 5.3 (a) to Fig. 5.2 (c), high resemblance is found between the porous microstructure composed of C/Pt agglomerates. Figure 5.3 (b) from the side view shows the non-uniformity of the C/Pt agglomerates deposition. Commonalities in terms of drying physics exist between spraying and drop drying. Spraying can be considered as many drops impinging and drying on the substrate. In the next section, real time drying dynamics of ink drop will be presented to explain the non-uniform microstructure formation.
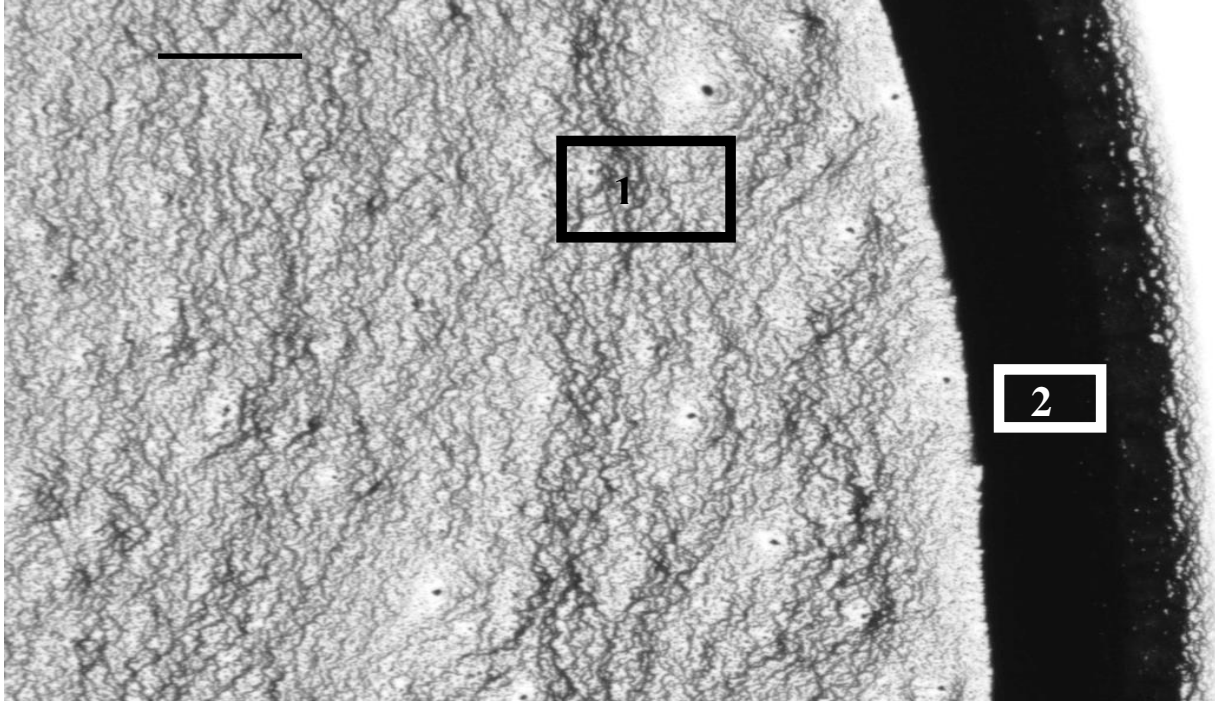
Fig 5.2 (a) Magnified image of the pattern in the rectangles shown in Fig 5.1. The scale bar denotes 100 µm
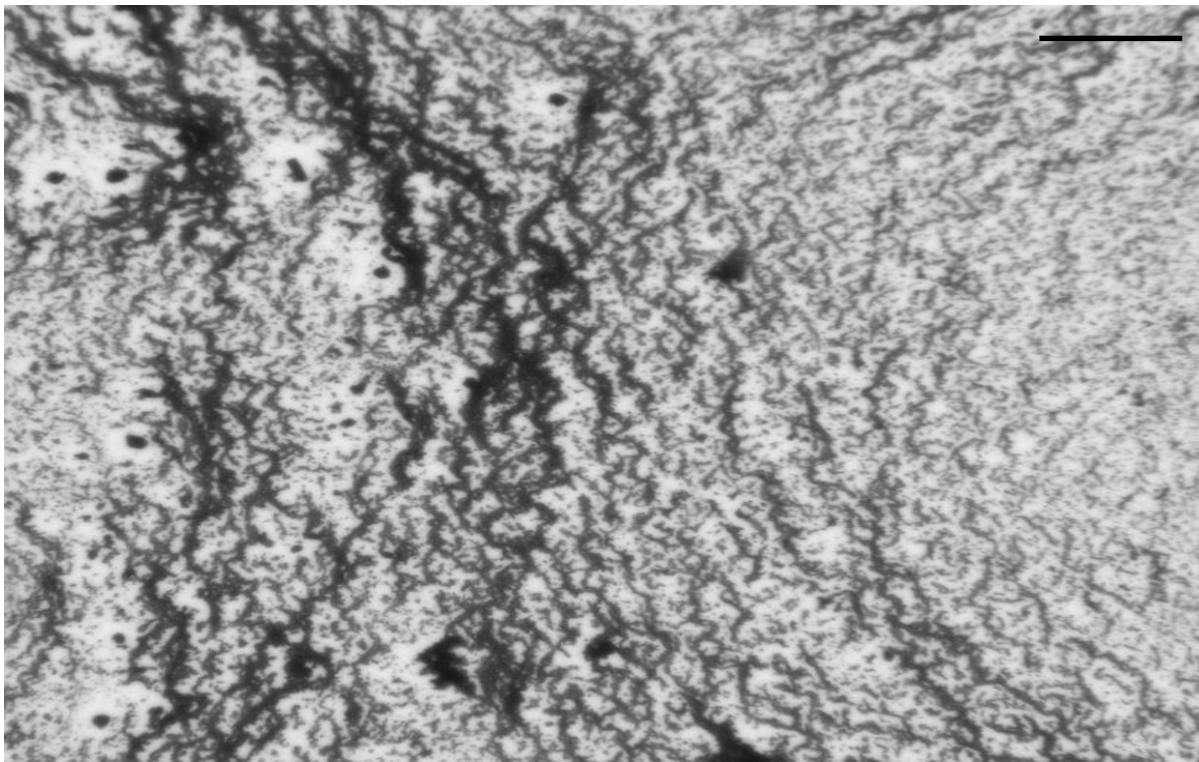


Fig 5.2 (b) C/Pt aggregates deposition at the inner region, which represents the pattern of rectangular 1 in Fig 5.2 (a). The scale bar denotes 20 µm.
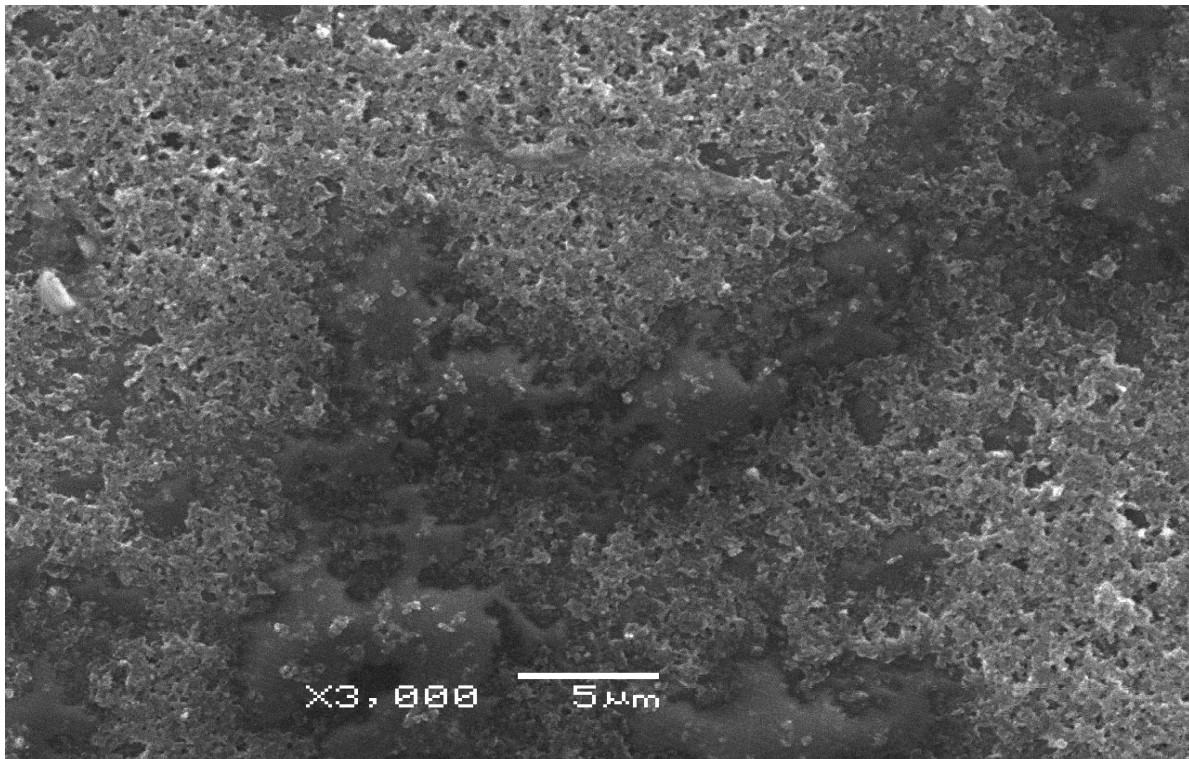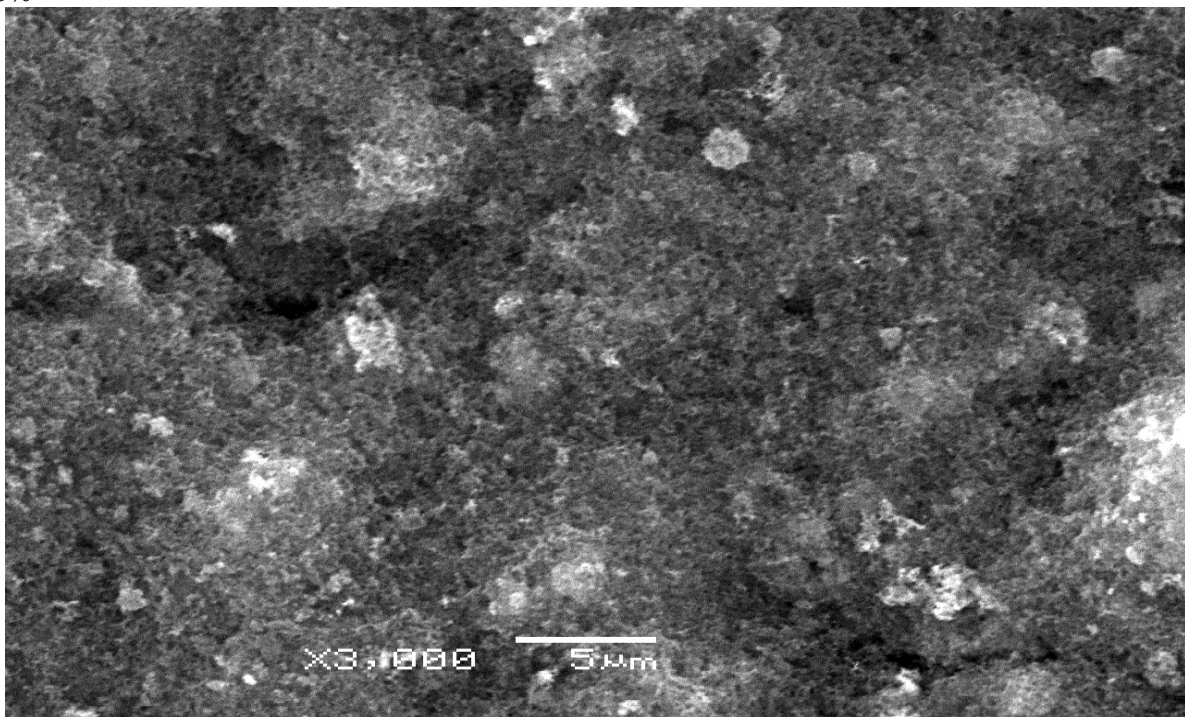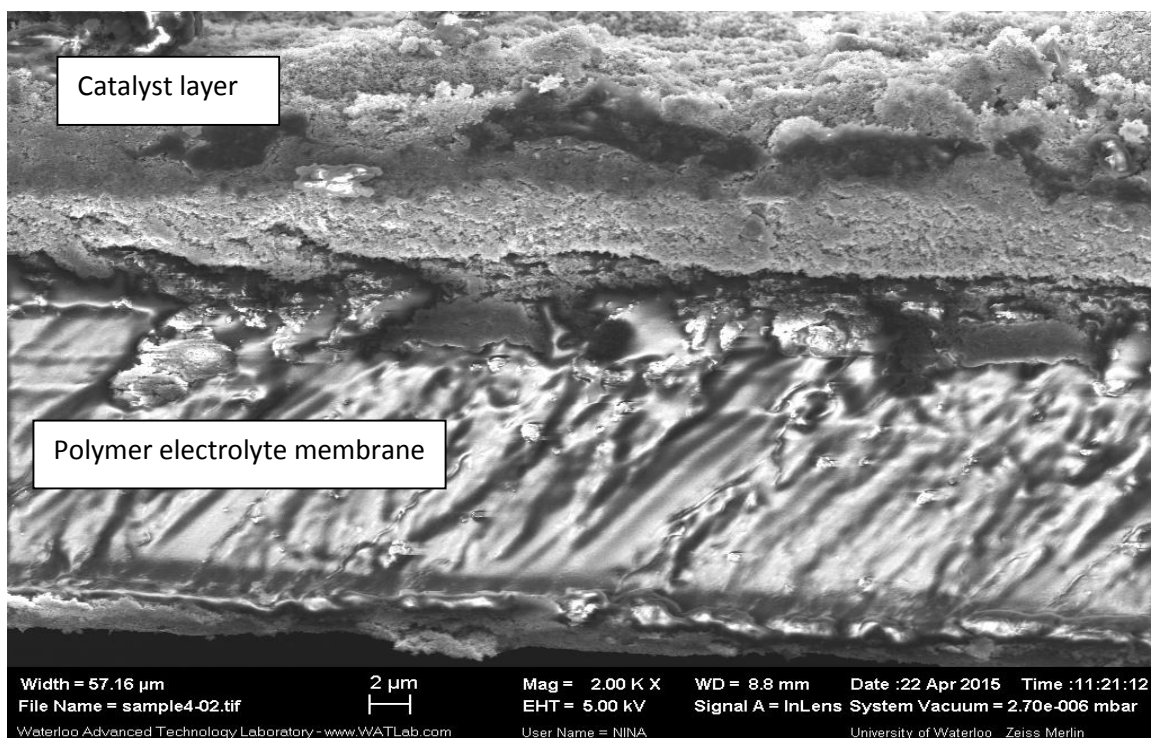
Fig 5.2 (c) Surface morphology of the pattern on the coffee-ring region marked by the rectangular 2 on the coffee-ring of $W_{Nafion}/W_{Nafion+C/Pt}$ = 25% (SEM).

Fig 5.2. Surface morphology of coffee-ring and microstructure of the inner region of $W_{Nafion}/W_{Nafion+C/Pt}$ = 25%



(a) Surface morphology of the CL made using spraying technique

(b) Through-plane of the CL made using spraying[3]

Fig 5.3. SEM of freshly made catalyst layer using spraying method ($W_{\text{Nafion}}/W_{\text{Nafion+C/Pt}} = 25\%$).
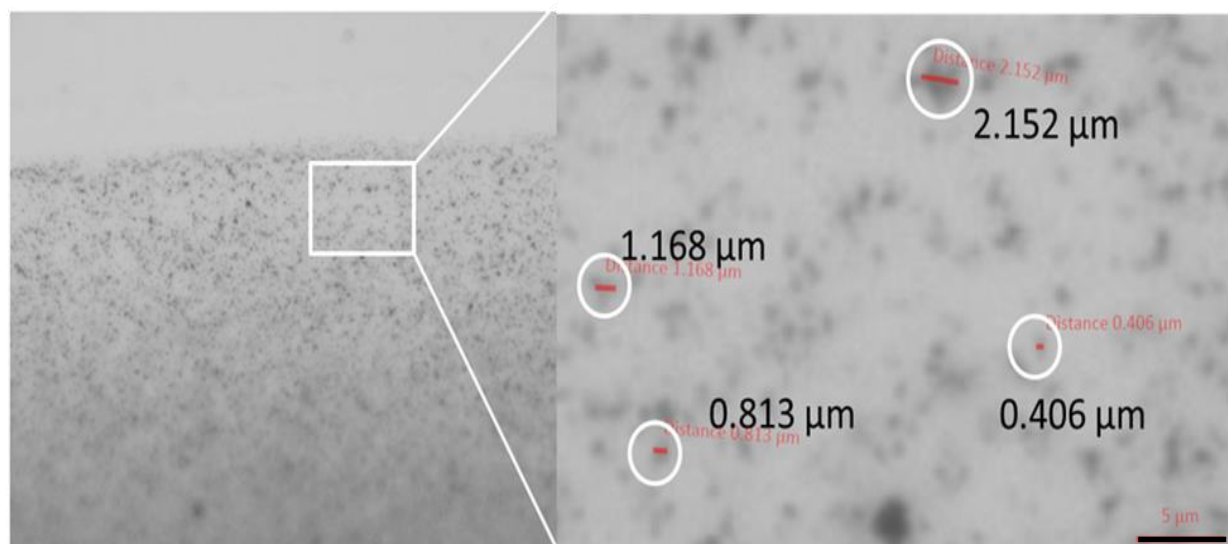
## 5.1.2 Drying dynamics



Fig 5.4. Heterogeneous C/Pt aggregates are dispersed in the solution observed under optical microscopy using backlighting. The scale bar denotes 5 μm.

---

[3] This SEM image is taken by samane shahgaldi, a researcher in the same group.

By focusing at the contact line with the thinnest thickness under the optical microscopy, it can be observed that the heterogeneous C/Pt aggregates with wide range of size (hundreds of nm to several µm) are dispersed into the drop shown in Fig. 5.4. Figure 5.5 shows that catalyst ink drop is drying out on the microscopy glass slide in two stages: contact line pinning and shrinking. The C/Pt aggregates flush toward the contact line, and pin and form coffee-ring there (Fig 5.5. (a)). Then the contact line shrinks inward quickly and finally the drop dries out, the C/Pt aggregates deposit at the edge to form into the connected deposition as the contact line shrinks inward (Fig 5.5. (b)).

A reversed flow which drags particles flushing toward the edge back to the center is observed and marked by the arrow directing inward in the magnified picture of Fig. 5.5 (a). The reversed flow occurs when the contact line is still advancing and continues after it pins. Those reversed particles collide with the outward particles to form a darker circle in the center of the drop shown in Fig. 5.5 (b). According to the criterion for the circulation flow direction given in Chapter 4, in our case[4], $k_{\text{iso-propanol}} = 0.13 \pm 0.01$ Wm$^{-1}$K$^{-1}$, $k_{\text{glass}} = 1.45 \pm 0.10$ Wm$^{-1}$K$^{-1}$, hence $k_R = k_{\text{glass}}/k_{\text{iso-propanol}} = 1.38/0.13 = 11.15$, would be sufficicently larger than correspnding $k_R^{crit}$ whose value is smaller than 2 shown in Fig. 4.6. Therefore the circulation direction should follow the one above the curve shown in Fig. 4.6, in which the flow first goes outward from the bottom, then the reversed flow goes inward back to the center along the air-liquid interface.

In the next section, the Nafion loading of the catalsyt ink will be varied to investigate its effect on the drying dynamcis and dried microstrucure deposition of the ink drops. From above obeservatoin and analysis, it is found that the reversed flow is triggered by the temperautrue-gradient over the drop, which is closely associated to the shape of the sessile drop, in another

---

[4] Perry's Chemical Engineer' Handbook, 7th ed; McGraw-Hill: New York, 1997.

words, the contact angle, as the drying condition is maintained. The contact angle is determiend by the liquid-solid-air triple phase interaction at the contact line [96], more specifically, the surface properties of the substrate, and the physicochemical properties of the solution. In our study, the physico-chemcial property of the catalyst ink varies as the Nafion content is varied, thus leading to the variaiton in the contact angle and resultant drying dyanmics.
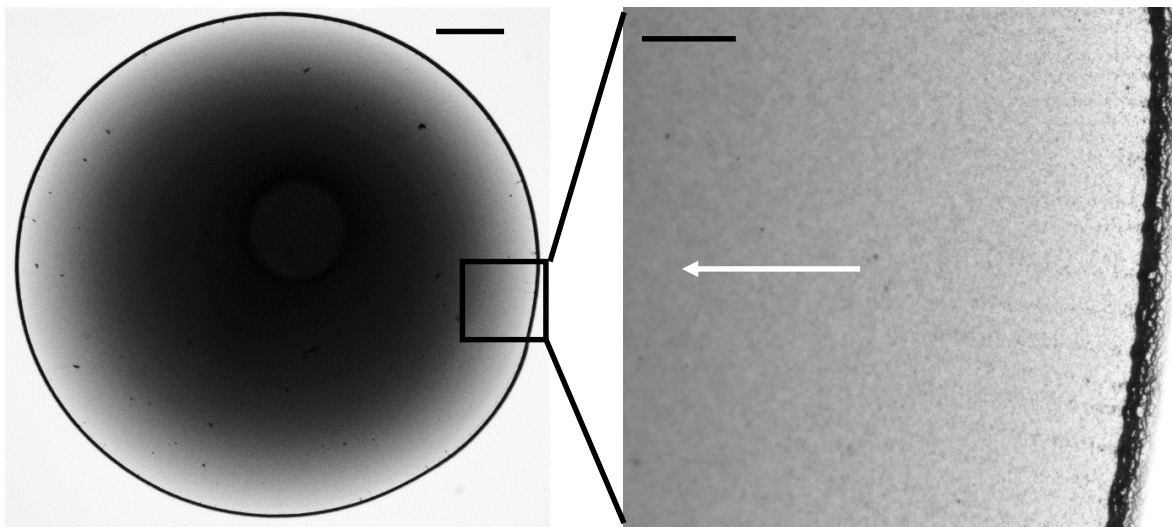


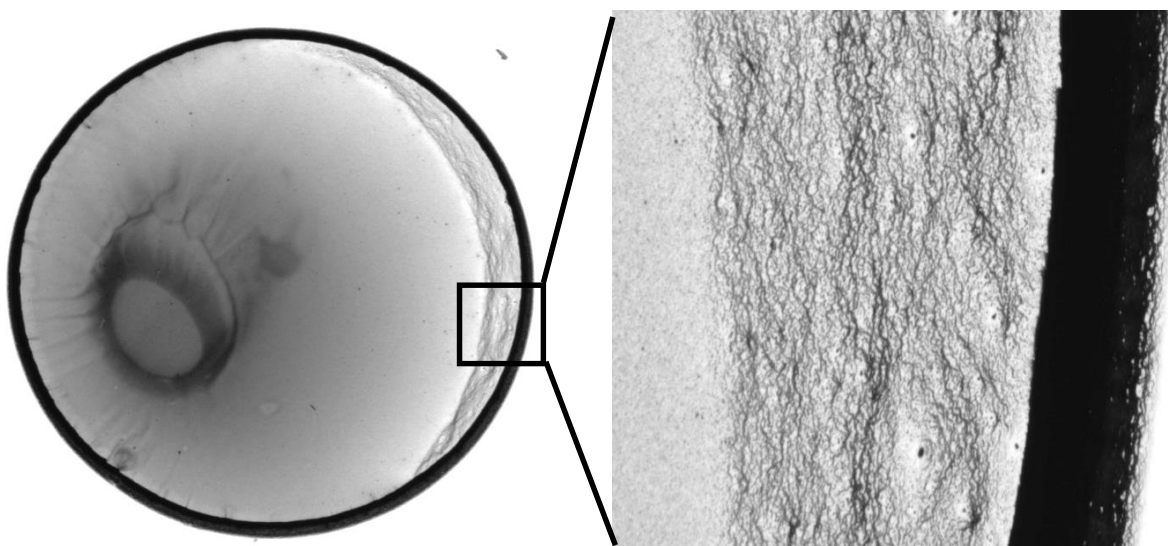Fig 5.5. (a) Particles flush toward and accumulate at the edge (stage 1)



Fig 5.5. (b) Contact line shrinks inward (stage 2)

Fig 5.5. Drying dynamics of $W_{Nafion}/W_{Nafion+C/Pt} = 25\%$ observed using backlighting. (a) The particles flush toward and accumulate at the edge (stage 1); (b) the contact line shrinks inward (stage 2). The scale bar in left figure of (a) denotes 500 µm, right figure of (b) denotes 100 µm.

## 5.2 Effect of Nafion content on microstructure formation ($W_{Nafion}/W_{Nafion+C/Pt} = 6.25\%$, 25 %, 62.5%)

According to Table 1 in Chapter 2, the Nafion loading is varied from the lowest, 15.5 % [14], to the highest, 50 % [23]. In our study, using $W_{Nafion}/W_{Nafion+C/Pt} = 25\%$ presented above as a reference point, the Nafion loading of 6.25%, 25 %, 62.5% are chosen as representative points to cover the Nafion loading available in the literature. As the Nafion content is changed, the contact angle and shape change accordingly when the drop sits on the substrate, and finally lead to various dried pattern.

### 5.2.1 Dried pattern

Figure 5.6 shows, from (a) to (c), the dried patterns of the ink drops of $W_{Nafion}/W_{Nafion+C/Pt} = 6.25\%$, 25%, and 62.5%, respectively. The diameter of the drop decreases as the Nafion loading is increased; the diameter for $W_{Nafion}/W_{Nafion+C/Pt} = 6.25\%$, 25 %, and 62.5% are 5.5 mm, 5.1 mm, and 4.5 mm, respectively.



(a) $W_{Nafion}/W_{Nafion+C/Pt} = 6.25\%$      (b) $W_{Nafion}/W_{Nafion+C/Pt} = 25\%$     (c) $W_{Nafion}/W_{Nafion+C/Pt} = 62.5\%$
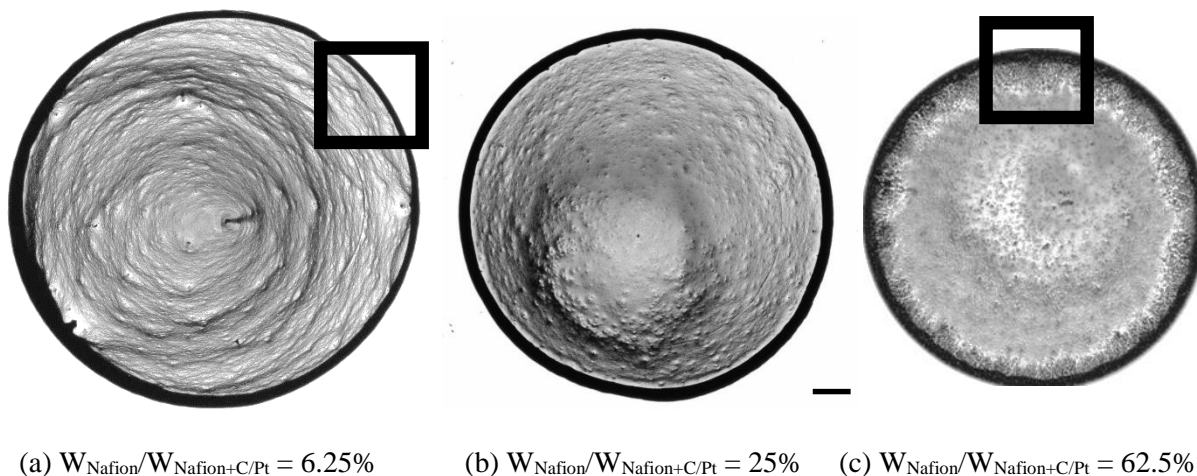
Fig 5.6. Dried patterns of the catalyst ink with varied Nafion content. The scale bar denotes 500 µm.

Figure 5.7 shows the thickness profiles of C/Pt aggregates deposition of the three dried ink samples. General tendency is shown that as the Nafion content is increased the particles are more uniformly distributed across the dried pattern. The ratio of the average thickness of the deposition of the inner region to the thickest part of the pattern increases: $W_{Nafion}/W_{Nafion+C/Pt} =$ 6.25 % is around 0.2, $W_{Nafion}/W_{Nafion+C/Pt} = 25$ % is around 0.4, and $W_{Nafion}/W_{Nafion+C/Pt} = 62.5$ % is around 0.5. The ratio of the width of the coffee-ring to the diameter of the drop also increases (Fig. 5.7 (a) – (c)).

Besides the significant change in the macro pattern shown in Fig. 5.7, the microstructure pattern also varies accordingly comparing to the reference point, $W_{Nafion}/W_{Nafion+C/Pt} = 25$ %. As shown in Fig. 5.8, is the magnified image for the window marked in Fig. 5.6. (a), for $W_{Nafion}/W_{Nafion+C/Pt} = 6.25$ %, the particles inside the edge deposit in a more connected form which takes on the concentric-ring patterns directed toward the center of the drop. As the Nafion content is increased, as shown in Fig. 5.9, with $W_{Nafion}/W_{Nafion+C/Pt} = 62.5$ %, pedal-like patterns directed inward are aligned at the inner side of the coffee-ring, and C/Pt aggregates inside edge, though most of which are still slightly connected via narrow bridges (marked by those arrows in the right figure of Fig. 5.9 (c)), are more dispersed instead of being tightly connected.

(a) $W_{Nafion}/W_{Nafion+C/Pt} = 6.25\%$.



(b) $W_{Nafion}/W_{Nafion+C/Pt} = 25\%$

41
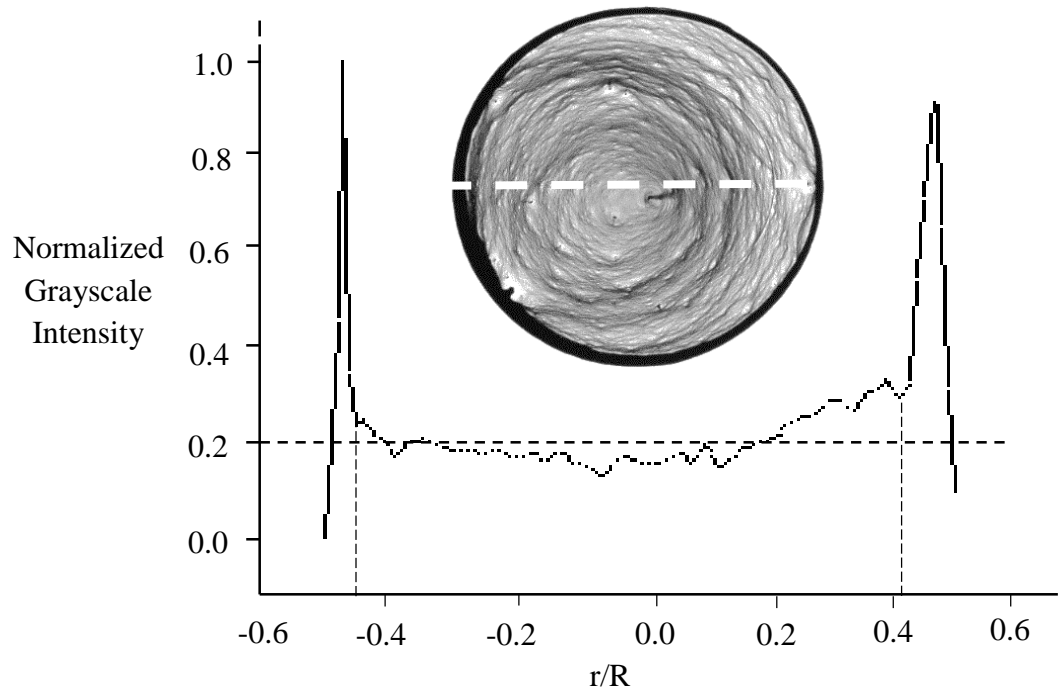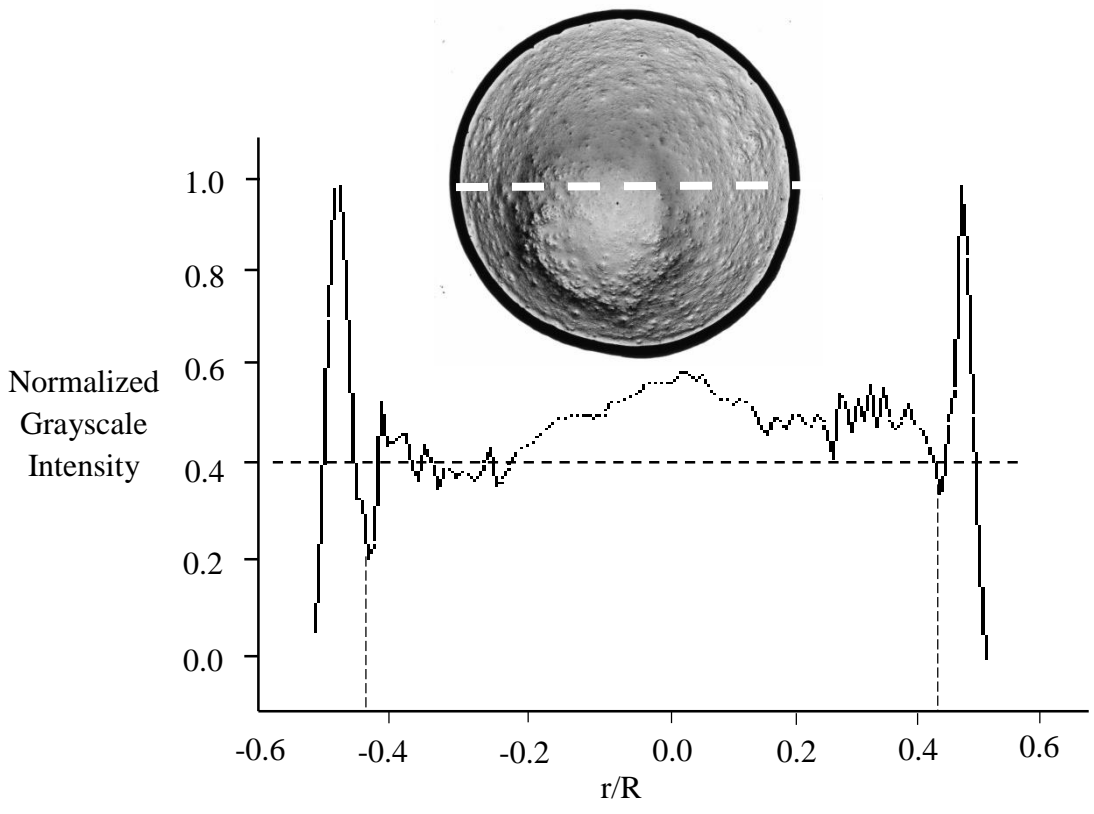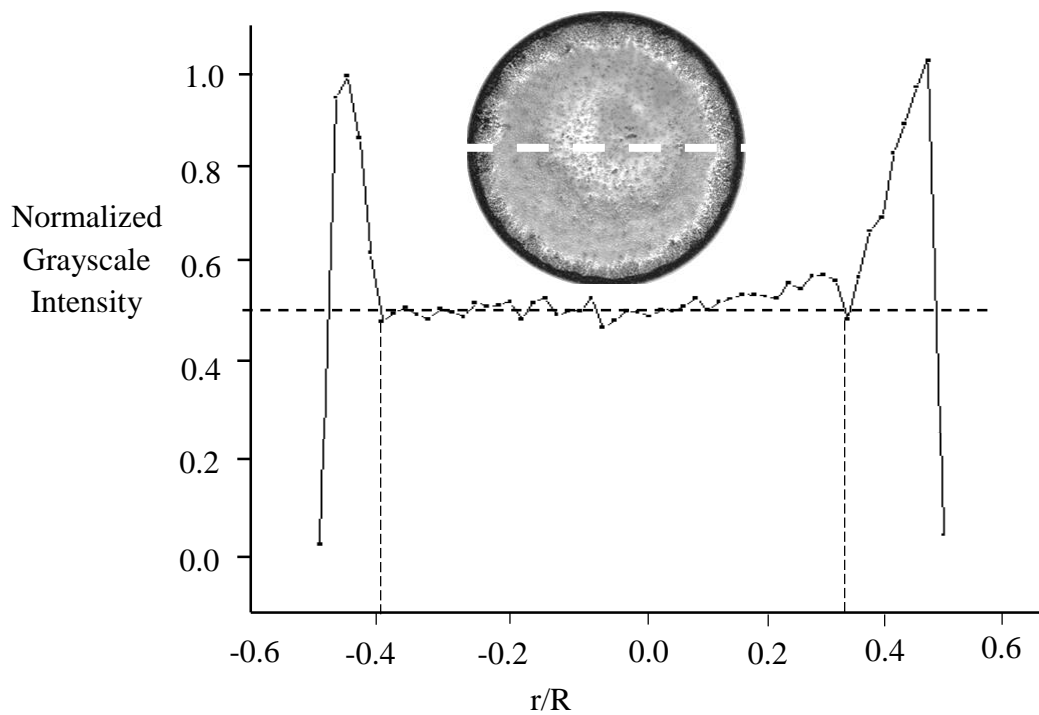
(c) $W_{Nafion}/W_{Nafion+C/Pt} = 62.5\%$

Fig 5.7. Thickness profiles of C/Pt aggregates deposition of the three dried ink samples, which is acquired by normalizing inverted grayscale intensities along the radial line of each sample. In those figures, the area marked out by the deposition line and two perpendicular dash lines is the deposition of the inner region, and the rest is the coffee-ring. The horizontal dash line denotes the average thickness of the deposition of the inner region.

(a)



(b)

Fig 5.8. Microstructure of the dried ink sample of $W_{Nafion}/W_{Nafion+C/Pt}$ = 6.25%. (a) The magnified picture of the rectangular shown in Fig. 5.6 (a) of $W_{Nafion}/W_{Nafion+C/Pt}$ = 6.25%. (b) The deposition of C/Pt aggregates inside the edge takes on the pattern of the concentric ring. The scale bar in the upper pic denotes 100 μm, the one in the bottom pic denotes 10 μm.
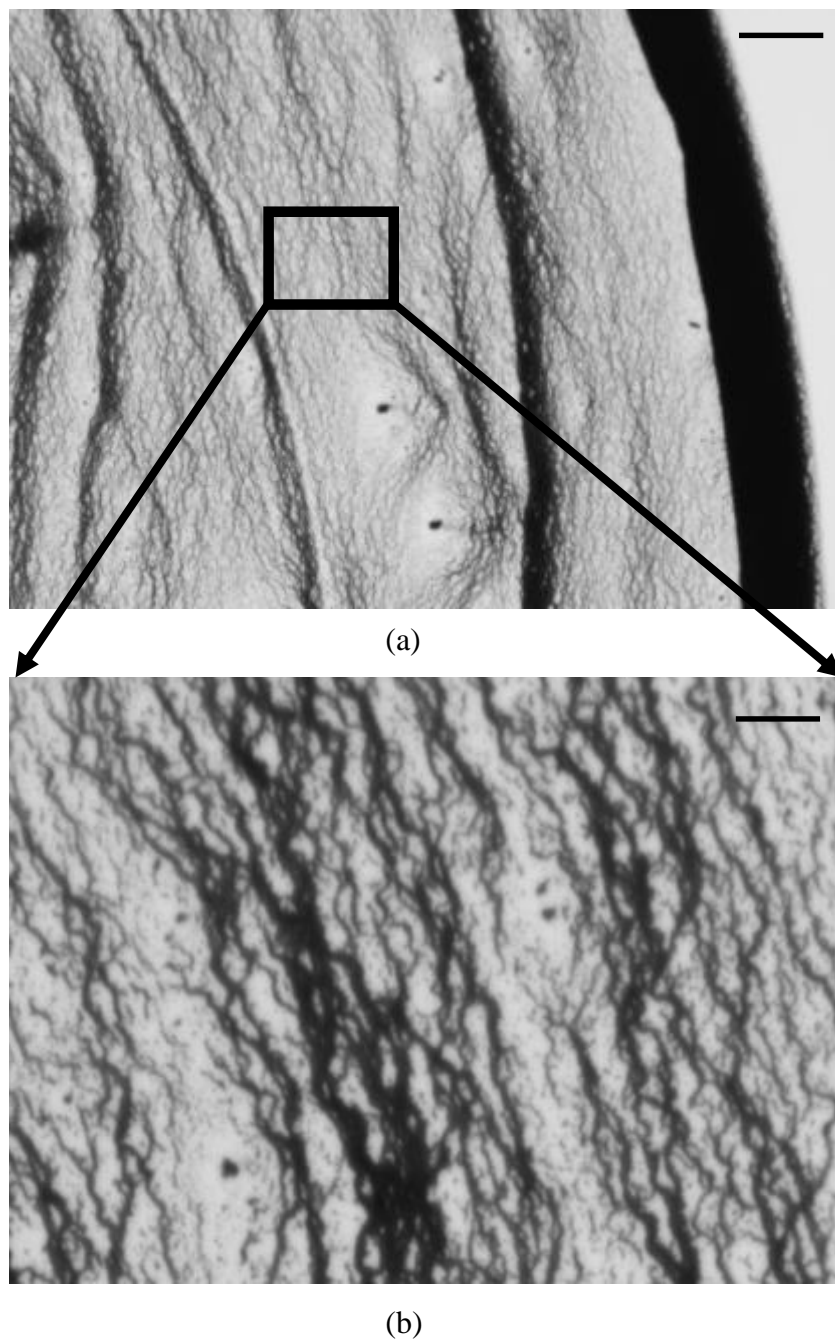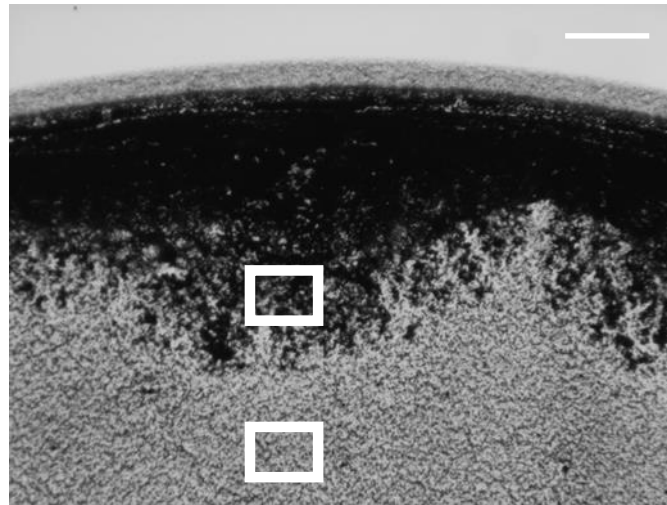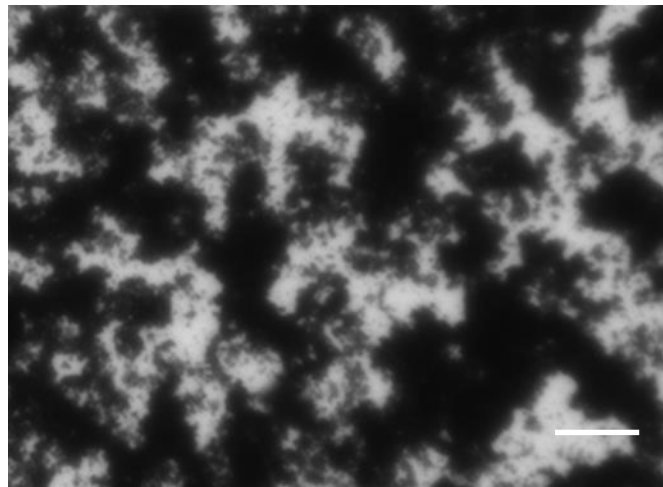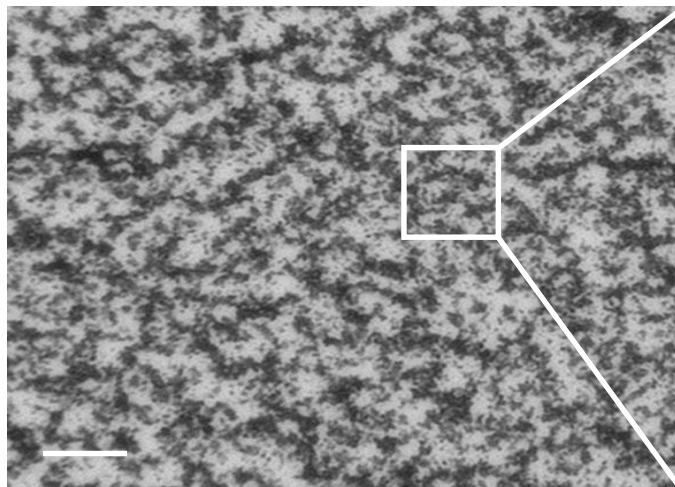
(a)



(b)



(c)

44

Fig 5.9. Microstructure of the dried ink sample for $W_{Nafion}/W_{Nafion+C/Pt} = 62.5\%$. (a) The magnified picture of the rectangular on the dried sample of $W_{Nafion}/W_{Nafion+C/Pt} = 62.5\%$, which shows a pedal-like pattern deposition. The deposition becomes more dispersed as going to the center, shown in (b) and (c). The scale bar in (a) denotes 200 μm, the one in (b) denotes 30 μm, the one in left pic of (c) denotes 30 μm, and the one in the right pic of (c) denotes 5 μm.



(a)
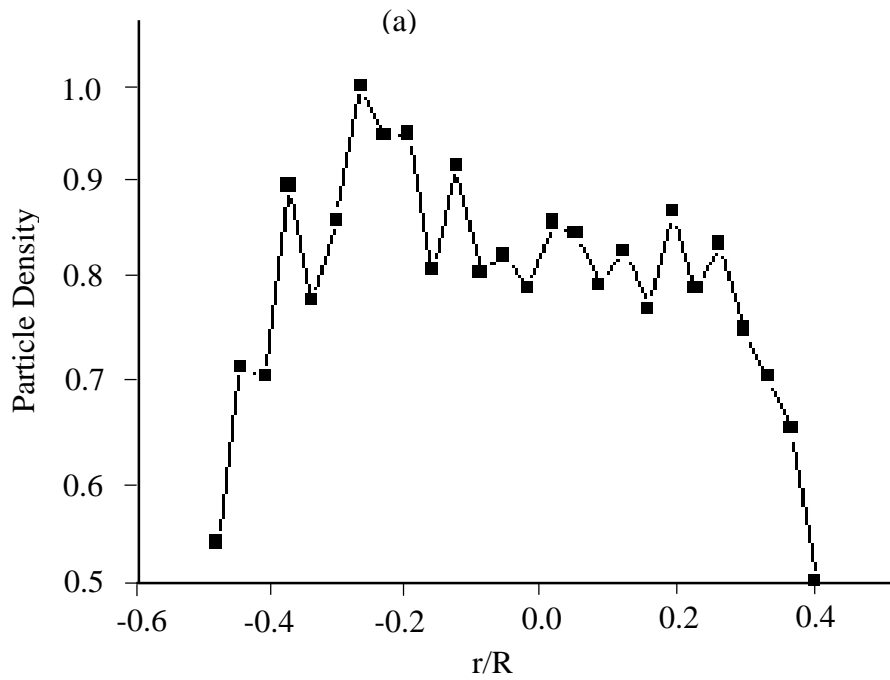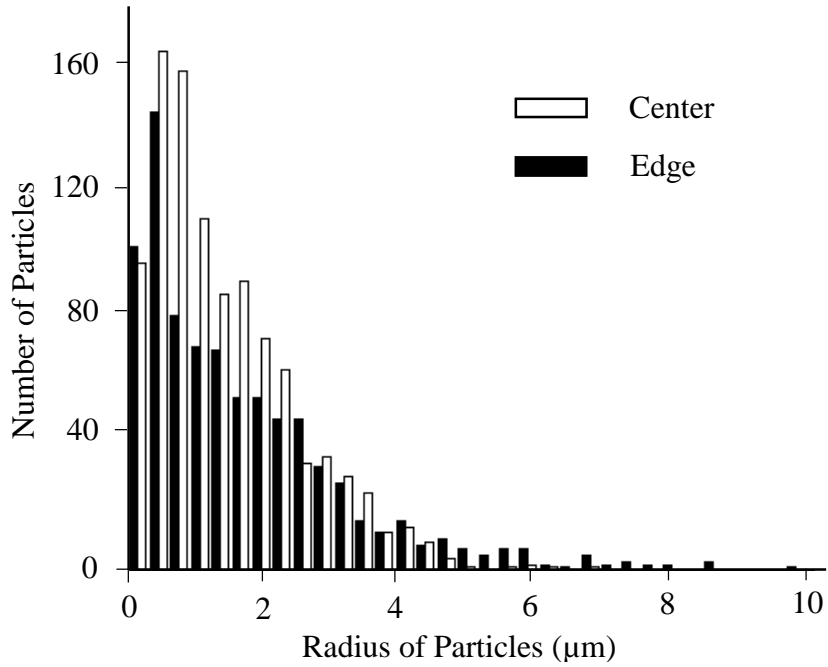


(b)

Fig 5.10. Particles size distribution (PSD) analysis for the dispersed C/Pt agglomerates of $W_{Nafion}/W_{Nafion+C/Pt} = 62.5\%$. (a) The PSD of dispersed C/Pt aggregates of two sample windows taken nearby the edge and at the center, respectively. (b) Particles density increases from the edge to the center of the dried sample.

Specifically, for $W_{Nafion}/W_{Nafion+C/Pt} = 62.5\%$, the average size of the dispersed particles decreases (Fig. 5.10 (a)) and the dispersion density increases (Fig. 5.10 (b)) along the line across the center, which indicates that the average particles size decreases, but the number of the dispersion increases as approaching the center of the drop. It should be noted that those dispersions are highly heterogeneous and slightly connected via narrow bridges, and need to be separated into pieces by cutting at those bridges for PSD analysis. For details of the image processing for the macro and micro pattern, readers are referred to the appendix for details.

5.2.2 Effect of drying dynamics on the dried pattern

As the Nafion content is increased, the whole drying time counted from the contact line pinning to the final drying out increases, as well as the ratio of the duration of the first stage to the whole drying time. As shown in Fig. 5.11 (a), the total drying time for $W_{Nafion}/W_{Nafion+C/Pt} = 6.25\%$ is around 48s, the first stage accounts for around 50% of the total drying time; for $W_{Nafion}/W_{Nafion+C/Pt} = 25\%$ it is around 55s, the first stage accounts for around 70%; whereas for $W_{Nafion}/W_{Nafion+C/Pt} = 25\%$ it is around 60s, the first stage accounts for around 90%. In the first pinning stage, the contact line is still slowly moving, and much lower than the second shrinking stage. As the Nafion loading is increased, the increased time in the pinning stage also explains the increase in the coffee-ring width that the width for $W_{Nafion}/W_{Nafion+C/Pt} = 6.25\%$ is smaller than 100 μm, the width for $W_{Nafion}/W_{Nafion+C/Pt} = 25\%$ is slightly larger than 100 μm, and the width for $W_{Nafion}/W_{Nafion+C/Pt} = 62.5\%$ is larger than 200 μm. Fig. 5.11 (b) is the non-dimensionalized counterpart for the diameters decreasing over time of the three samples.

The drying dynamics also varies significantly as the Nafion content is varied. Figure 5.12 gives the snapshots of drying dynamics at t = 0.0 $t_{whole}$, 0.2 $t_{whole}$, 0.4 $t_{whole}$, 0.6 $t_{whole}$, 0.8 $t_{whole}$ for the three samples. For $W_{Nafion}/W_{Nafion+C/Pt}$ = 6.25% shown in Fig. 5.12 (a), a web-like pattern appears in the center of the drop and reversed flow is not observed. For $W_{Nafion}/W_{Nafion+C/Pt}$ = 25% shown in Fig. 5.12 (b), reversed flow occurs and collides with the outward flow to form a dark circle; small vortices aligning at the edge are observed as the drying proceeds to later stage (t = 0.4 $t_{whole}$ (row 3)). As the Nafion content continues to be increased to $W_{Nafion}/W_{Nafion+C/Pt}$ = 62.5% shown in Fig. 5.12 (c), besides the reversed flow and resultant dark circle, jet-like vortices with uniform distance appear at the edge (t = 0.2 $t_{whole}$ (row 2)), the magnified vortices in the rectangle is shown in Fig. 5.13; those vortices continue to enlarge and merge into bigger vortices (t = 0.4 $t_{whole}$ (row 3), t = 0.6 $t_{whole}$ (row 4), t = 0.8 $t_{whole}$ (row 5)), then eventually dry out and deposit into the pedal-like patterns shown in Fig. 5.9 (a).
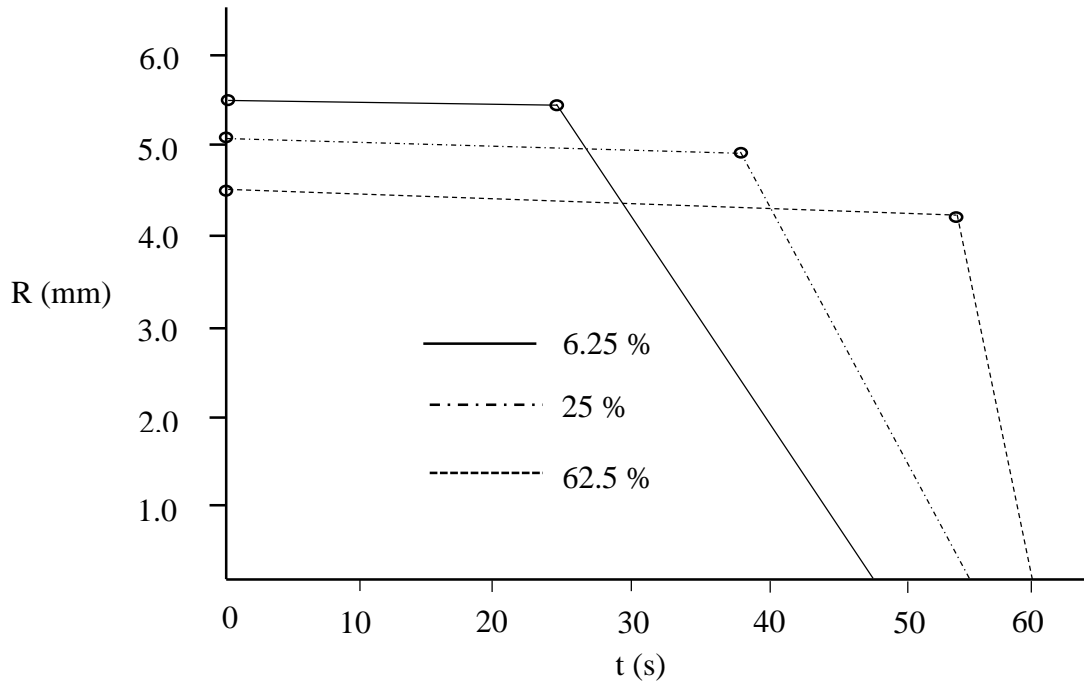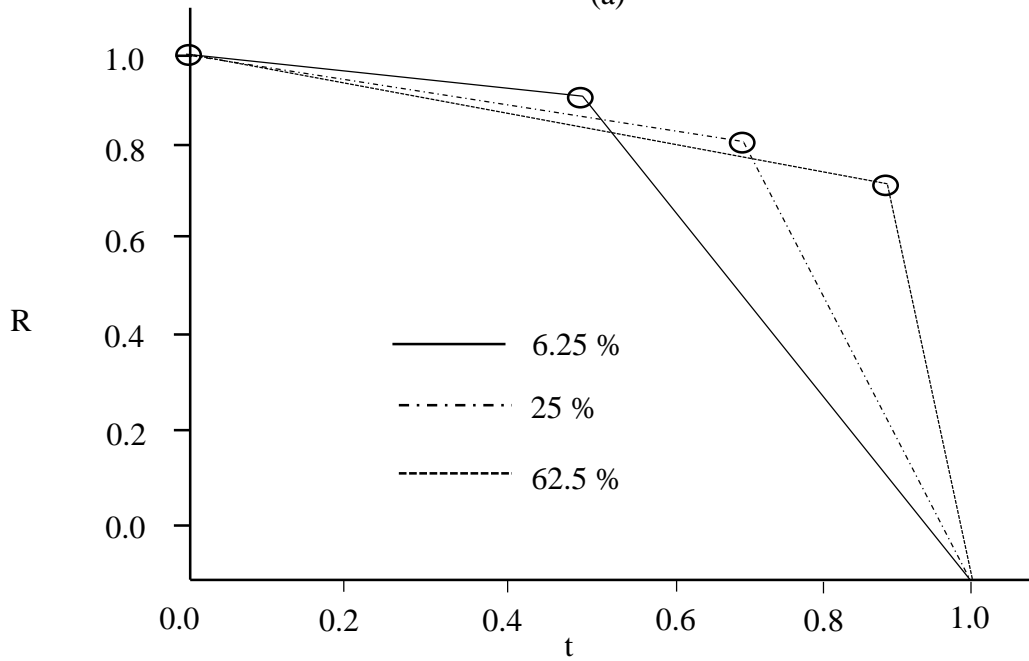
Fig 5.11. Contact line radius, R, of wetting drop changes with time for the three samples. Each sample are composed of two lines, which represent first contact line pinning and second contact line shrinking stage. (a) Dimensionalized one. (b) Non-dimensionalized one. The t and R are both non-dimensionalized by dividing by its total drying time and initial pinned diameter, respectively.

(a) $W_{Nafion}/W_{Nafion+C/Pt} = 6.25\%$  (b) $W_{Nafion}/W_{Nafion+C/Pt} = 25\%$  (c) $W_{Nafion}/W_{Nafion+C/Pt} = 62.5\%$
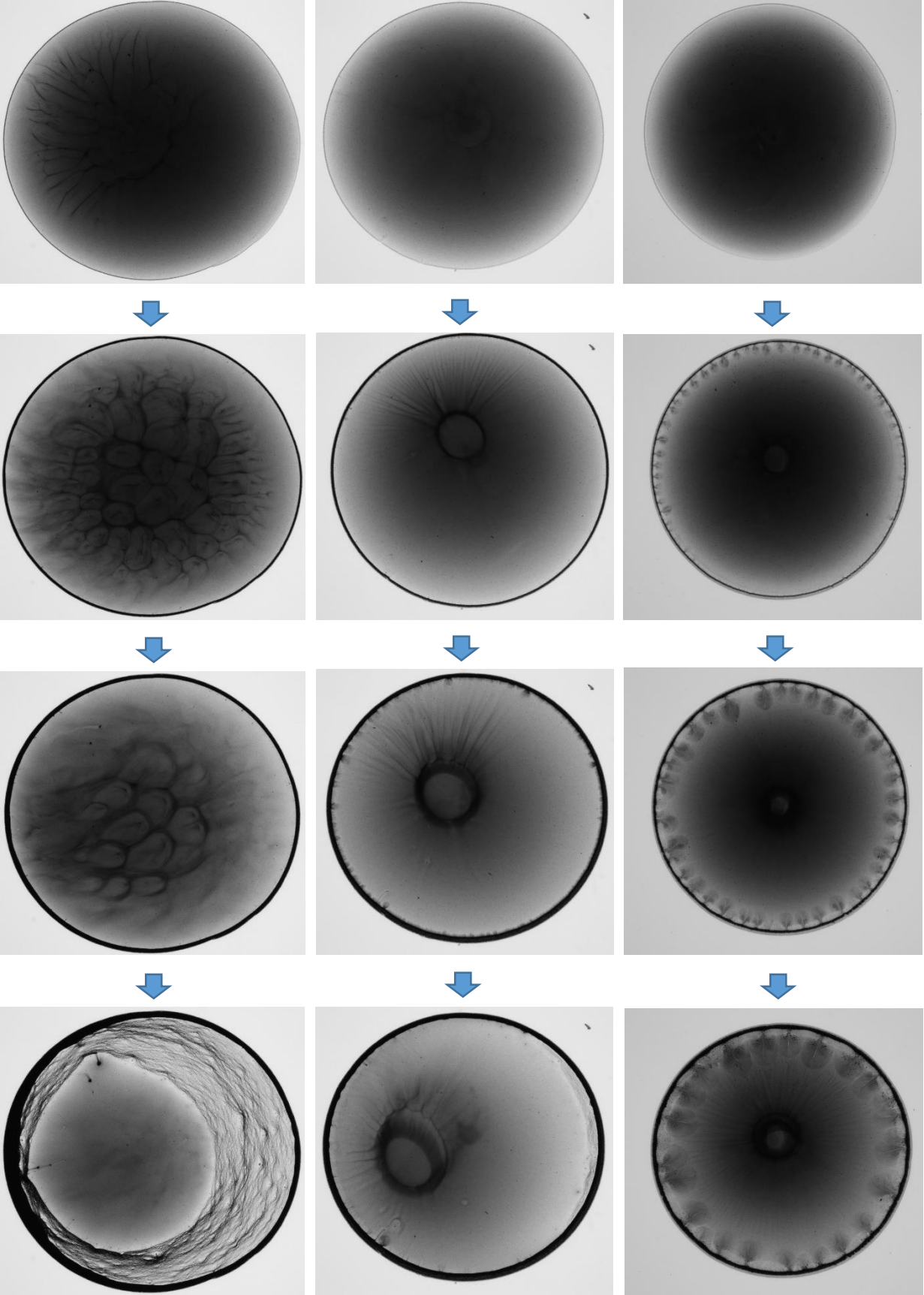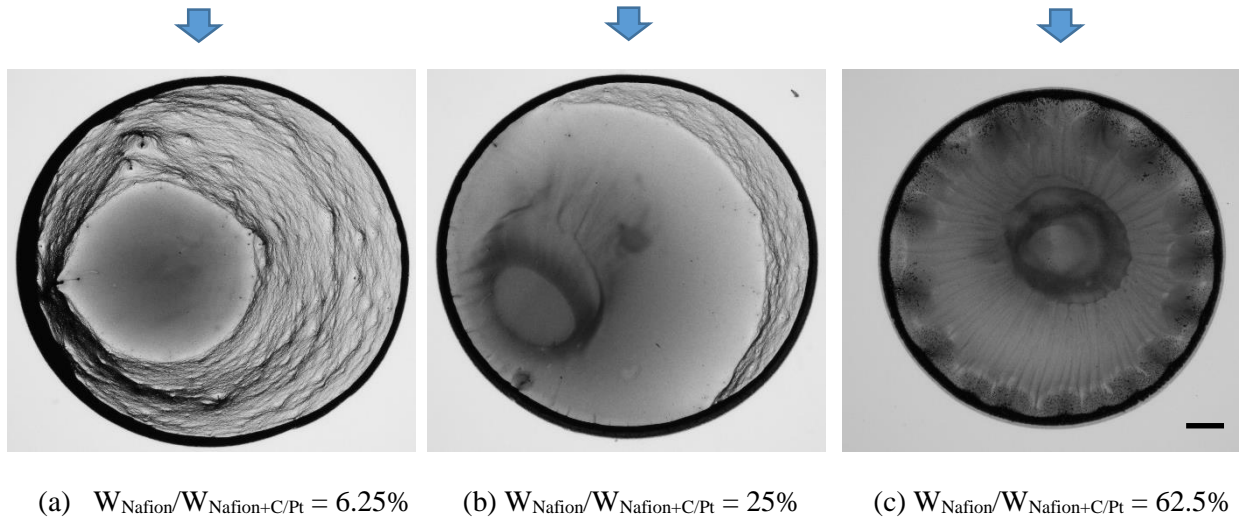
Fig 5.12. Snapshots of the drying dynamics of the three samples at t = 0.0 $t_{whole}$ (row 1), 0.2 $t_{whole}$ (row 2), 0.4 $t_{whole}$ (row 3), 0.6 $t_{whole}$(row 4), 0.8 $t_{whole}$(row 5). The scale bar at the bottom right corner denotes 500 μm.
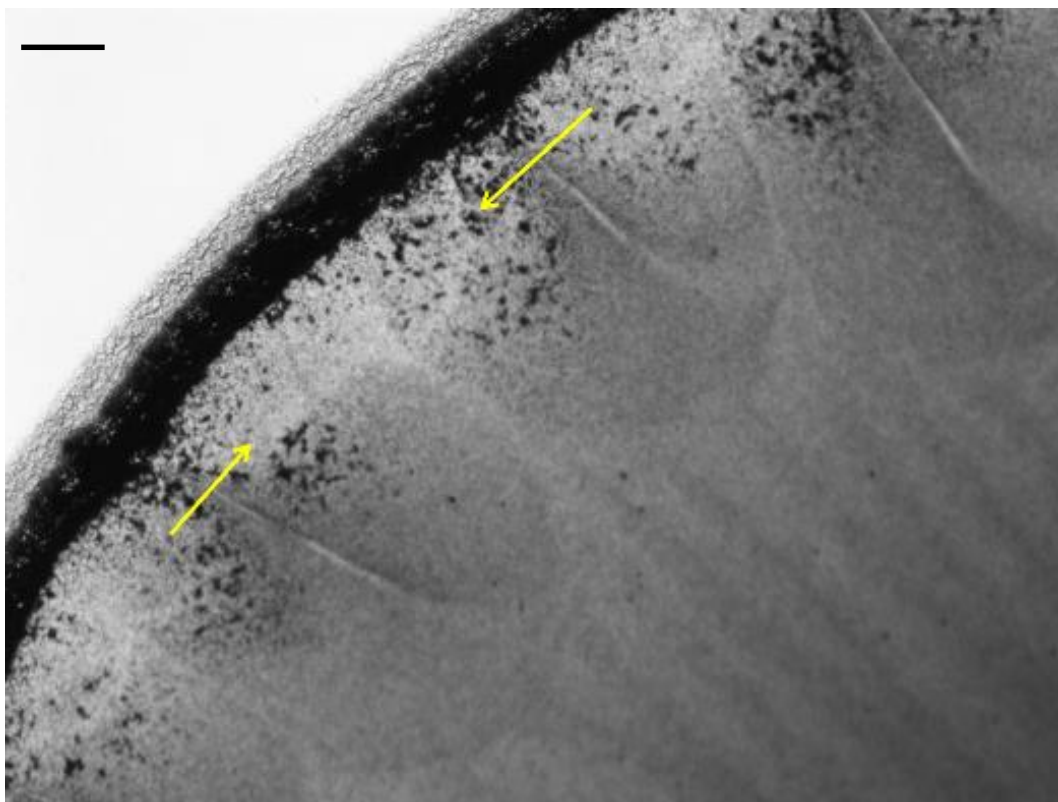


Fig 5.13. Jet vortices form at the edge are observed in the drying drop; for $W_{Nafion}/W_{Nafion+C/Pt} = 62.5\%$, these vortices grow and merge into larger eddies as evaporation occurs. The arrows denote that the vortices are moving as they grow. The scale bar denotes 100 μm.

This significant distinction of the drying dynamics can be attributed to the shape of the sessile drop when they initially pin. As shown in Fig. 5.14, the side view profile of sessile drop shape becomes more curved as the Nafion content is increased. By magnifying the area marked in the circle shown in Fig. 5.14, the contact angle are measured to be $11.6^o$, $14.5^o$, and $17.0^o$ for $W_{Nafion}/W_{Nafion+C/Pt} = 6.25\%$, $25\%$, and $62.5\%$, respectively.

The change in shape is associated with the change in the liquid/air surface tension of the liquid as the Nafion loading is varied. As mentioned in Chapter 4, the capillary length, $K^{-1} = \sqrt{\sigma/\rho g}$, is a gauge for whether the sessile drop takes on a curved shape or a puddle [97]. Measured by the Dataphysics DCAT 11, figure 5.15 shows the surface tension of the catalyst ink, $\sigma_{la}$, increases as the Nafion content is increased: for $W_{Nafion}/W_{Nafion+C/Pt} = 6.25$ % (Nafion concentration is 0.32 mg/ml), $\sigma = 20.82 \pm 0.01$ mN/m; for $W_{Nafion}/W_{Nafion+C/Pt} = 25$ % (Nafion concentration is 4.17 mg/ml), $\sigma = 20.95 \pm 0.01$ mN/m; for $W_{Nafion}/W_{Nafion+C/Pt} = 62.5$ % (Nafion concentration is 8.03 mg/ml), $\sigma = 21.10 \pm 0.01$ mN/m. Therefore the capillary length also increases accordingly as the change in density can be negligible ($\rho_{\text{iso-propyl}}$ [5] $= 0.795$ g/cm$^3$, $g = 9.8$ m/s$^{-2}$). For $W_{Nafion}/W_{Nafion+C/Pt} = 6.25$ %, the gravitational force dominates over capillary force; as the Nafion loading is increased, the capillary force gradually dominates the gravitational force which enables the drop to develop a more curved shape as shown in Fig. 5.14.

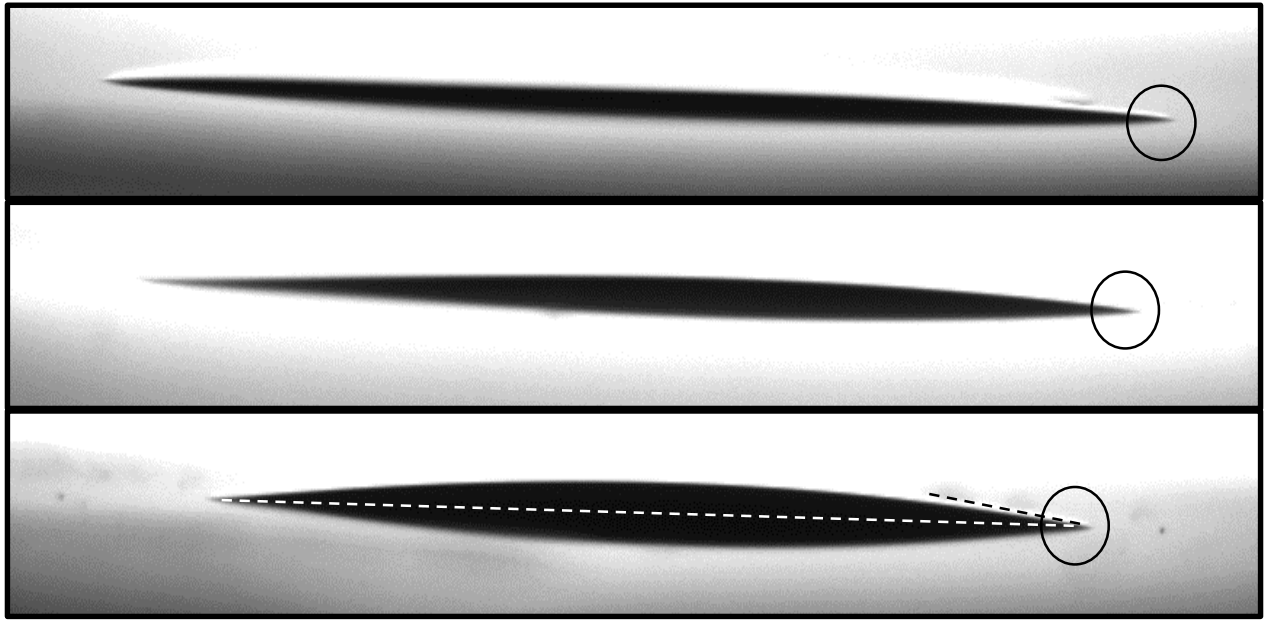[5] Perry's Chemical Engineer' Handbook, 7th ed; McGraw-Hill: New York, 1997

Fig 5.14. Side view of the drop when it initially pins. From upper to bottom, $W_{Nafion}/W_{Nafion+C/Pt} = 6.25\%$, 25%, and 62.5%, respectively. The diameters are 5.5 mm, 5.1 mm, 4.5 mm respectively.
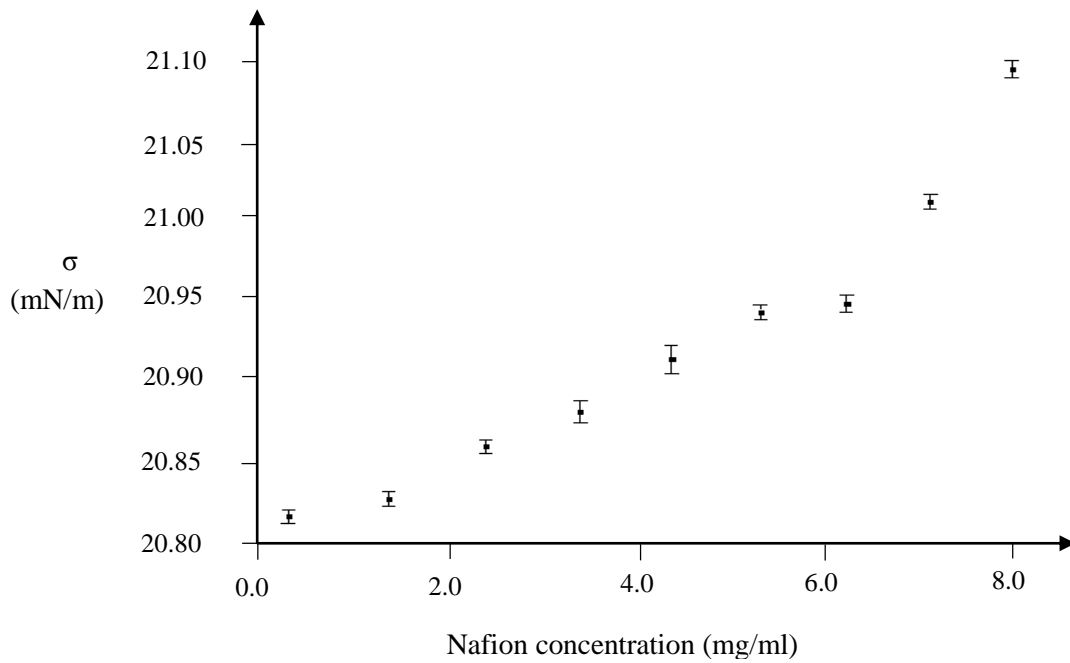


Fig 5.15. Surface tension of the catalyst ink, as measured in this study, increases as the Nafion loading is increased.
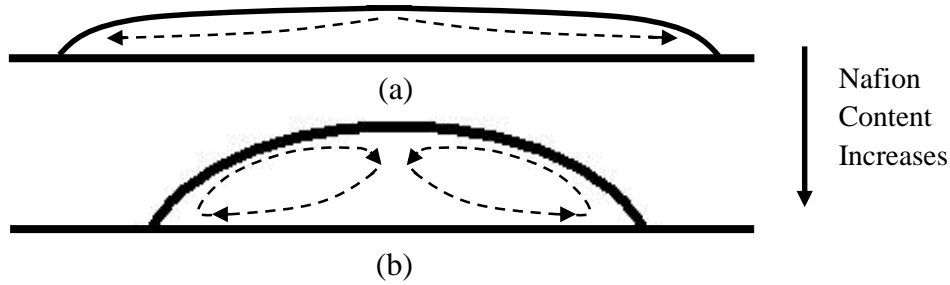
(a)

(b)

Nafion
Content
Increases

Fig 5.16. Schematics of the changes in the internal flow direction of the drying drop as the shapes change

As illustrated in Fig. 5.16, the catalyst drop becomes more curved as its Nafion loading is increased. Figure 5.16 (a) shows that the sessile drop takes on the shape of a puddle which corresponds to $W_{Nafion}/W_{Nafion+C/Pt} = 6.25\%$. The reversed flow is not activated due to insufficient surface tension gradient from the edge to the apex of the drop; instead a web-like pattern appears in the center shown in Fig. 5.12. The web-like pattern is Benard-Marangoni (BM) cell, which is driven by thermos-capillary flow on the plane of the drop surface and was first studied by Scriven et al. [98] in 1956. Capillary length is also an indicator for whether the BM cell can be triggered. Only as $h \leq K^{-1}$, the BM cell can be triggered, where h is the thickness of the thin film, $K^{-1}$ is the capillary length of this fluid. In our case, h is around 100 μm, and is sufficiently smaller than its capillary length (5 mm). As the Nafion loading is increased, the sessile drop bulges on the substrate and a reversed flow which flows outward along the substrate and inward along the liquid/air interface is incurred in the drop as shown in Fig. 5.16 (b). As the Nafion loading is increased to $W_{Nafion}/W_{Nafion+C/Pt} = 62.5\%$, the contact line pinning stage dominates the whole drying process. C/Pt aggregates continue to circulate in the drop along the reversed flow, and eventually leads to the widest coffee-ring and dispersed deposition at the inner region.

For $W_{Nafion}/W_{Nafion+C/Pt} = 62.5\%$, a series of jet vortices are activated, whose occurrence and evolution result in grand petal-like stains at the edge. The occurrence, enlargement, and merging of the jet vortices are found in a previous colloidal drop study, which is termed as Marangoni

vortices, and is attributed to the three-dimensional hydrothermal waves in the wedge near the contact line [87]. The initial wave structure on the free surface is well-illustrated by focusing on the edge as the contact line is advancing using top lighting shown in Chapter 3 (Fig. 3.2 (c)). In order to capture the flow inside the drop, the backlighting is still used for the advancing movement as well as the vortices evolvement afterwards. As shown in Fig. 5.17, when the contact line is advancing, an interference pattern is observed on the surface of the particle-free wedge film and indicates the surface undulation; beads of drops forming at the fringe of the edge are being pushed outward simultaneously (shown in the rectangle in Fig. 5.17 (a)). As the contact line initially pins, beads detach from the solute-free fringe, and the fringe quickly dries inward. The hydrothermal waves are activated from the initial surface undulation, and continue to involve into larger waves shown in Fig. 5.17 (b). For details regarding the vortices evolvement, readers are referred to the Fig. B1 in appendix.



100 µm
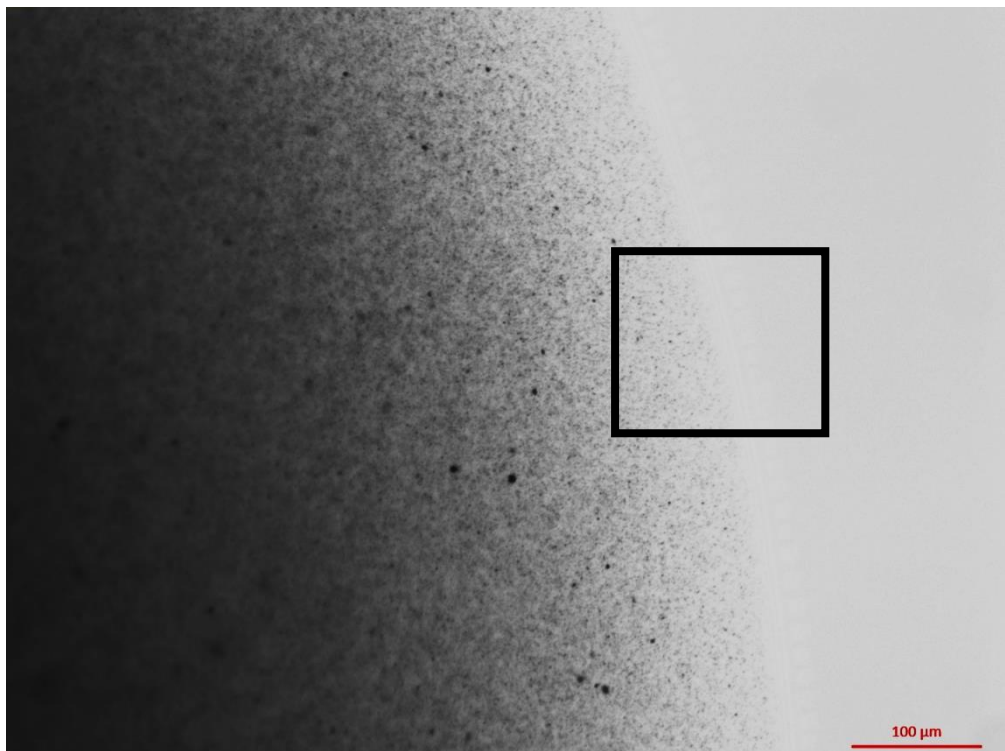
(a)
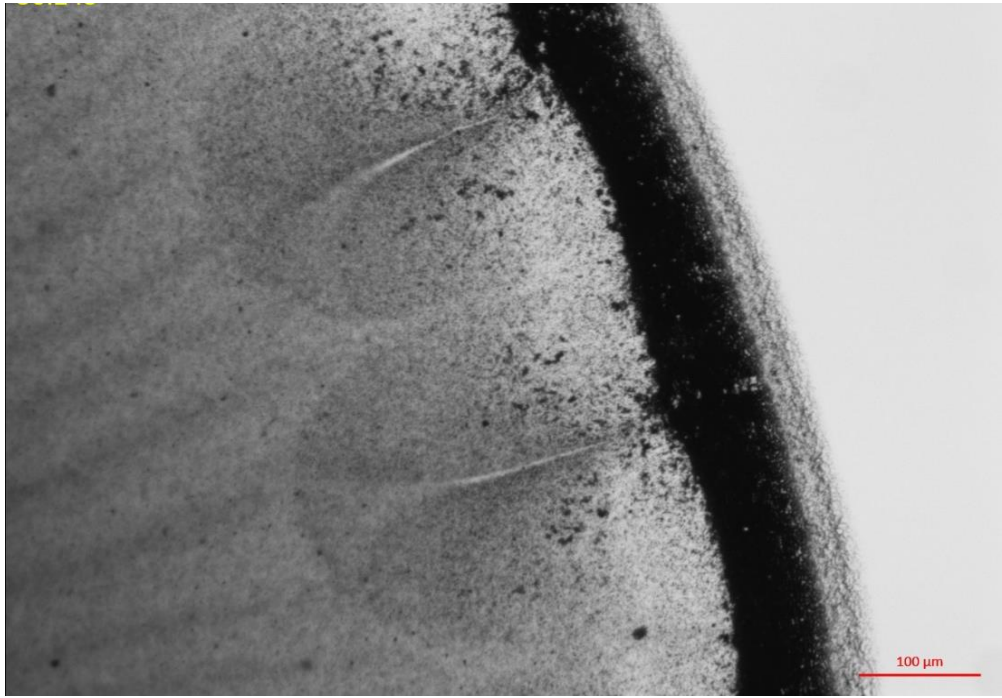
(b)

Fig 5.17. Contact line dynamics and its wave structure on the free surface as the drop is spreading, for $W_{Nafion}/W_{Nafion+C/Pt} = 62.5\%$. (a) As the drop is spreading up, the interference pattern on the edge and beads around the edge highlight the surface undulation of the wedge film. (b) Evolving into vortices. The rectangle at the edge is magnified to the picture at the right bottom corner, which is binarized to demonstrate the interference pattern. The scale bar denotes 100 μm.

Sobac et al. and Sefiane et al. both observed 3D hydrothermal waves in the region near the contact line of evaporating sessile drop without solute [99][100], which provide qualitative support to the Marangoni vortex evolvement in our study. Sobac et al. proposed that the number of vortices decreases nonlinearly with time; while Sefiane et al. proposed that the wave number decreases linearly with time. In Fig. 5.18, the length of the wave, the distance between the roots of two neighboring vortices, increases linearly with time; this indicates that the wave number decreases linearly with time, as is our case. The thickness of the drop decreases as the wave number decreases over time, therefore the temperature gradient along the free surface near contact line decreases and eventually fails to provide sufficient driving force for the wave

55

involvement. It also helps to explain that the vortices are not activated in the case of $W_{Nafion}/W_{Nafion+C/Pt} = 25\%$ for its limited thickness near the contact line.



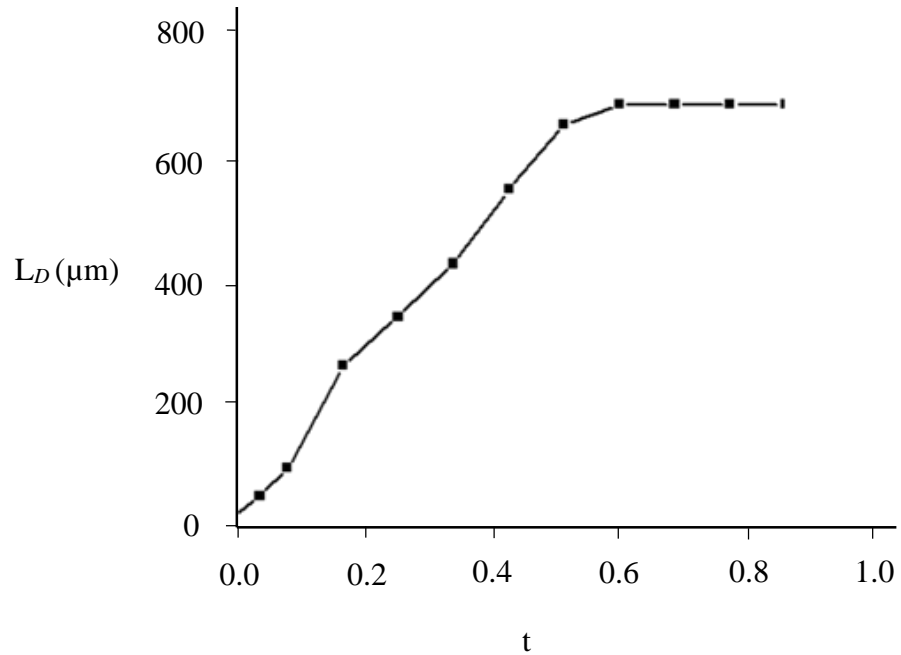Fig 5.18. Distance between the roots of the neighboring vortices, $L_D$, increases linearly with time, $W_{Nafion}/W_{Nafion+C/Pt} = 62.5\%$. t is non-dimensional by dividing the whole evaporation time.

# Chapter 6 Conclusions and Recommendations

6.1 Conclusions

This study improves the fundamental understandings of the effect of drying dynamics on the microstructure formation of catalyst layer by investigating the microstructural formation through catalyst ink drop drying, with a focus on the effect of the variation in Nafion loading.

First, the results show that Nafion loading has a significant impact on the C/Pt aggregate deposition of the dried drop. The ink sample with NPF = 25%, the most commonly used catalyst ink composition for industrial CL fabrication, is first studied. Its dried pattern composes of a dense coffee-ring at the edge and a very diluted but connected C/Pt aggregates inside the edge. As the Nafion loading is decreased, the C/Pt aggregates are more condensed at the edge and the rest are aligned in the form of concentric ring pattern toward the center. In contrast, as the Nafion loading is increased, C/Pt aggregates are more uniformly distributed over the whole drop, and are dispersed in the form of heterogeneous detached aggregates inside the edge. Besides, unique pedal-like pattern with uniform distance align along the inner side of the coffee ring.

Secondly, the significant variations in micro- and macro- pattern of the dried drops are resulted from changes in the drying dynamics of the drop evaporation as the Nafion loading is varied. The internal flow and relevant C/Pt agglomerates transport and deposition is dictated by surface tension variation on the free surface of the drying drop due to the evaporative cooling. As the evaporating condition (e.g. $T$, $P$, $RH$) and surface properties of the substrate are maintained (e.g. hydrophilic glass slide), the physicochemical properties of the solution dictate the drying profile and hence the heat and mass transfer on the drop. The drop with low Nafion loading flattens, so outward convective flow dominates and brings particles to the edge to form a dense coffee ring. As the Nafion content is increased, the shape of the sessile drop is more bended; this induces a

surface tension gradient that drives the fluids in the upper layer to flow backwards, thus setting up a flow circulation in the drop. As the Nafion content continues to increase, the shape of the drop bends more; besides reversed flow, three-dimension thermo-capillary waves induce equally spaced Marangoni vortices along the contact line, leading to pedal-like pattern at the edge. Inside the edge, the deposition are more dispersed into heterogeneous C/Pt aggregates with equivalent circular size of on the order of μm, due to continuous circulation along the reversed flow.

6.2 Recommendations

CL fabrications, cell assembly, and performance tests need to be incorporated to find out baseline ink composition with optimum NPF (the ratio of Nafion to C/Pt by weight). Then based on the baseline ink composition, the solvent drying condition for the catalyst ink drops evaporation needs to be appropriately modified, e.g. the physico-chemical property of the solution, the substrate interfacial property, or the drying condition, to achieve a desirable microstructure deposition, e.g. more uniform deposition.

More advanced microstructure characteristics are needed, e.g. non-uniform thickness, non-uniform local concentration, and non-uniform local morphology, to connect the factors determining the initial microstructure, e.g. ink composition and preparation, and fabrication process, to the macro-properties of the deposition, e.g. porosity, electronics and protonic conductivity, and diffusive coefficient. The improved understanding of the effect of drying dynamics on the final microstructure from the small volume catalyst ink drying can serve to be a guidance to optimize the CL fabrication technique, thus eventually to increase the catalyst utilization.

# References

[1]     B. D. James and A. B. Spisak, "Mass Production Cost Estimation of Direct H 2 PEM Fuel Cell Systems for Transportation Applications", pp. 1–62, 2012.

[2]     Y. Wang, K. S. Chen, J. Mishler, S. C. Cho, and X. C. Adroher, "A review of polymer electrolyte membrane fuel cells: Technology, applications, and needs on fundamental research," *Appl. Energy*, vol. 88, pp. 981–1007, 2011.

[3]     DOE, "DOE Hydrogen and Fuel Cells Program: 2014 Annual Progress Report," 2014.

[4]     J. Zhang, PEM Fuel Cell Electrocatalysts and Catalyst Layers: Fundamentals and Applications. London: Springer, 2008.

[5]     S. Holdcroft, 'Fuel Cell Catalyst Layers: A Polymer Science Perspective,' Chemistry of Materials 26 (1), pp. 381-393, 2014.

[6]     P. K. Das, X. Li, and Z.-S. Liu, "A three-dimensional agglomerate model for the cathode catalyst layer of PEM fuel cells," *J. Power Sources*, vol. 179, pp. 186–199, 2008.

[7]     D. Susac, and V. Berejnov, "STXM Characterization of PEM Fuel Cell Catalyst Layers," *ECS Trans.*, vol. 50, pp. 405–413, 2012.

[8]     S. Wessel., "DE-EE0000466 Final Project Report Development of Micro-Structural Mitigation Strategies for PEM Fuel Cells : Morphological Simulations and Experimental Approaches," 2013.

[9]     P. K. Das, X. Li, and Z.-S. Liu, "Analysis of liquid water transport in cathode catalyst layer of PEM fuel cells," *Int. J. Hydrogen Energy*, vol. 35, pp. 2403–2416, 2010.

[10]    K. Artyushkova, S. Pylypenko, M. Dowlapalli, and P. Atanassov, "Structure-to-property relationships in fuel cell catalyst supports: Correlation of surface chemistry and morphology with oxidation resistance of carbon blacks," *J. Power Sources*, vol. 214, pp. 303–313, 2012.

[11]    T. Soboleva, "On the microstructure of PEM fuel cell catalyst layers," Ph.D. Thesis. Simon Fraser University, 2010.

[12]    T. Soboleva, X. Zhao, K. Malek, Z. Xie, T. Navessin, and S. Holdcroft, "On the micro-, meso-, and macroporous structures of polymer electrolyte membrane fuel cell catalyst layers.," *ACS Appl. Mater. Interfaces*, vol. 2, pp. 375–84, 2010.

[13]    S. Litster and G. McLean, "PEM fuel cell electrodes," *J. Power Sources*, vol. 130, pp. 61–76, 2004.

[14] M. Chaparro, J. Martín, M. Folgado, B. Gallardo, and L. Daza, "Comparative analysis of the electroactive area of Pt/C PEMFC electrodes in liquid and solid polymer contact by underpotential hydrogen adsorption/desorption," *Int. J. Hydrogen Energy*, vol. 34, pp. 4838–4846, 2009.

[15] X. Yuan, X.-L. Ding, C.-Y. Wang, and Z.-F. Ma, "Use of polypyrrole in catalysts for low temperature fuel cells," *Energy Environ. Sci.*, vol. 6, pp. 1105, 2013.

[16] S. Zhang, X.-Z. Yuan, J. N. C. Hin, H. Wang, K. A. Friedrich, and M. Schulze, "A review of platinum-based catalyst layer degradation in proton exchange membrane fuel cells," *J. Power Sources*, vol. 194, pp. 588–600, 2009.

[17] S. Kundu, M. W. Fowler, L. C. Simon, and S. Grot, "Morphological features (defects) in fuel cell membrane electrode assemblies," *J. Power Sources*, vol. 157, pp. 650–656, 2006.

[18] A. F. Routh, "Drying of thin colloidal films.," *Rep. Prog. Phys.*, vol. 76, 046603, 2013.

[19] L. W. Niedrach, "U. S. Patent 3," 297, 484, 1967.

[20] R. J. Lawrence, "U.S. Patent 4," 272, 353, 1981.

[21] S. J. Lee, S. Mukerjee, J. Mcbreen, Y. W. Rho, Y. T. Kho, and T. H. Lee, "Effect of Nafion on impregnation on performances of PEMFC electrodes," vol. 43, pp. 3693–3701, 1998.

[22] E. A. Ticianelli, C. R. Derouin, A. Redondo, and S. Srinivasan, "Methods to Advance Technology of Proton Exchange Membrane Fuel Cells," *J. Electrochem. Soc,* vol. 1, 1983.

[23] S. J. Lee, S. Mukerjee, J. Mcbreen, Y. W. Rho, Y. T. Kho, and T. H. Lee, "Effects of Nafion on impregnation on performances of PEMFC electrodes," *Electrochim. Acta,* vol. 43, 1998.

[24] M. S. Wilson and S. Gottesfeld, "Thin-film catalyst layers for polymer electrolyte fuel cell electrodes," *J. Appl. Electrochem.*, vol. 22, 1992.

[25] V. A. Paganin, E. A. Ticianelli, and E. R. Gonzalez, "Development and electrochemical studies of gas diffusion electrodes for polymer electrolyte fuel cells," *J. Appl. Electrochem.*, vol. 26, 1996.

[26] Y.-G. Chun, C.-S. Kim, D.-H. Peck, and D.-R. Shin, "Performance of a polymer electrolyte membrane fuel cell with thin film catalyst electrodes," *J. Power Sources*, vol. 71, pp. 174–178, 1998.

[27] J. M. Song, S. Y. Cha, and W. M. Lee, "Optimal composition of polymer electrolyte fuel cell electrodes determined by the AC impedance method," *J. Power Sources*, vol. 94, 2001.

[28]   Z. Qi and A. Kaufman, "Low Pt loading high performance cathodes for PEM fuel cells," *J. Power Sources*, vol. 113, pp. 37–43, 2003.

[29]   A. Fischer, J. Jindra, and H. Wendt, "Porosity and catalyst utilization of thin layer cathodes in air operated PEM-fuel cells," *Int. J. Hydrogen Energy*, vol. 28, pp. 277–282, 1998.

[30]   M. S. Wilson, J. A. Valerio, and S. Gottesfeld, "Low Platinum Loading Electrodes For Polymer Electrolyte Fuel Cells Fabricated Using Thermoplastic," *Electrochemica. Acta.* Vol. 40. pp. 355-363, 1995.

[31]   H.-S. Park, Y.-H. Cho, Y.-H. Cho, C. R. Jung, J. H. Jang, and Y.-E. Sung, "Performance enhancement of PEMFC through temperature control in catalyst layer fabrication," *Electrochim. Acta*, vol. 53, 2007.

[32]   J. Zhao, X. He, L. Wang, J. Tian, C. Wan, and C. Jiang, "Addition of NH4HCO3 as pore-former in membrane electrode assembly for PEMFC," *Int. J. Hydrogen Energy*, vol. 32, pp. 380–384, 2007.

[33]   M. S. Wilson and S. Gottesfeld, "Thin-film catalyst layers for polymer electrolyte fuel cell electrodes," *J. Appl. Electrochem.*, vol. 22, pp. 1–17, 1992.

[34]   M. Uchida, Y. Aoyama, N. Eda, and A. Ohta, "New Preparation Method for Polymer-Electrolyte Fuel Cells," *J. Electrochem. Soc*, vol. 142, pp. 463–468, 1995.

[35]   M. Uchida, Y. Fukuoka, Y. Sugawara, H. Ohara, and A. Ohta, "Improved Preparation Process of Very-Low-Platinum-Loading Electrodes for Polymer Electrolyte Fuel Cells," *J. Electrochem. Soc*, vol. 145, 1998.

[36]   S.-J. Shin, J.-K. Lee, H.-Y. Ha, S. -a. Hong, H.-S. Chun, and I.-H. Oh, "Effect of the catalytic ink preparation method on the performance of polymer electrolyte membrane fuel cells," *J. Power Sources*, vol. 106, pp. 146–152, 2002.

[37]   T.-H. Yang, Y.-G. Yoon, G.-G. Park, W.-Y. Lee, and C.-S. Kim, "Fabrication of a thin catalyst layer using organic solvents," *J. Power Sources*, vol. 127, pp. 230–233, 2004.

[38]   R. Fern, P. Ferreira-aparicio, and L. Daza, "PEMFC electrode preparation : Influence of the solvent composition and evaporation rate on the catalytic layer microstructure," *J. Power Sources*, vol. 151, pp. 18–24, 2005.

[39]   A. Therdthianwong, P. Ekdharmasuit, and S. Therdthianwong, "Fabrication and Performance of Membrane Electrode Assembly Prepared by a Catalyst-Coated Membrane Method: Effect of Solvents Used in a Catalyst Ink Mixture," *Energy & Fuels*, vol. 24, pp. 1191–1196, 2010.

[40]   D. Huang, P. Yu, F. Liu, S. Huang, and K. Hsueh, "Effect of Dispersion Solvent in Catalyst Ink on Proton Exchange Membrane Fuel Cell Performance," *Int. J. Electrochem. Sci,* vol. 6, pp. 2551–2565, 2011.

[41]   H.-S. Park, Y.-H. Cho, Y.-H. Cho, C. R. Jung, J. H. Jang, and Y.-E. Sung, "Performance enhancement of PEMFC through temperature control in catalyst layer fabrication," *Electrochim. Acta*, vol. 53, pp. 763–767, 2007.

[42]   X. Liang, G. Pan, L. Xu, and J. Wang, "A modified decal method for preparing the membrane electrode assembly of proton exchange membrane fuel cells," *Fuel*, vol. 139, pp. 393–400, 2015.

[43]   C. Hsu, "An innovative process for PEMFC electrodes using the expansion of Nafion film," *J. Power Sources*, vol. 115,  pp. 268–273, 2003.

[44]   T. Jao, G. Jung, H. Shen, C. Yeh, and Y. Su, "Ultrasonic Spray Coating for Proton Exchange Membrane Fuel Cell," *Open Journal of Acoustics,* vol. 3, pp. 33–37, 2013.

[45]   M. Chaparro, M. Folgado, P. Ferreira-Aparicio, J. Martín, I. Alonso-Álvarez, and L. Daza, "Properties of Catalyst Layers for PEMFC Electrodes Prepared by Electrospray Deposition," *J. Electrochem. Soc.*, vol. 157, pp. B993, 2010.

[46]   M. F. Weber, S. Mamiche-afara, M. J. Dignam, L. Pataki, and R. D. Venter, "Sputtered Fuel Cell Electrodes," *J. Electrochem. Soc.* vol. 86, pp. 1416–1419, 1987.

[47]   T. E. Experiment and M. Corporation, "High performance proton exchange membrane fuel cells with sputter-deposited Pt layer electrodes,"*Electrochimica Acta,* vol. 42, pp. 1587–1593, 1997.

[48]   S. Y. Cha and W. M. Lee, "Performance of Proton Exchange Membrane Fuel Cell Electrodes Prepared by Direct Deposition of Ultrathin Platinum on the Membrane Surface," *J. Electrochem. Soc*, vol. 146, pp. 4055–4060, 1999.

[49]   R. O'Hayre, S.-J. Lee, S.-W. Cha, and F. Prinz, "A sharp peak in the performance of sputtered platinum fuel cells at ultra-low platinum loading," *J. Power Sources*, vol. 109, pp. 483–493, 2002.

[50]   M. D. Gasda, R. Teki, T.-M. Lu, N. Koratkar, G. a. Eisman, and D. Gall, "Sputter-Deposited Pt PEM Fuel Cell Electrodes: Particles vs Layers," *J. Electrochem. Soc.*, vol. 156, pp. B614, 2009.

[51]   D. Fofana, J. Hamelin, and P. Bénard, "Modelling and experimental validation of high performance low platinum multilayer cathode for polymer electrolyte membrane fuel cells (PEMFCs)," *Int. J. Hydrogen Energy*, vol. 38, pp. 10050–10062, 2013.

[52]     N. Cunningham, E. Irissou, M. Lefèvre, M.-C. Denis, D. Guay, and J.-P. Dodelet, "PEMFC Anode with Very Low Pt Loadings Using Pulsed Laser Deposition," *Electrochem. Solid-State Lett.*, vol. 6, pp. A125, 2003.

[53]     M. S. Saha, A. F. Gullá, R. J. Allen, and S. Mukerjee, "High performance polymer electrolyte fuel cells with ultra-low Pt loading electrodes prepared by dual ion-beam assisted deposition," *Electrochim. Acta*, vol. 51, pp. 4680–4692, 2006.

[54]     N. Ramaswamy, T. M. Arruda, W. Wen, N. Hakim, M. Saha, a. Gullá, and S. Mukerjee, "Enhanced activity and interfacial durability study of ultra low Pt based electrocatalysts prepared by ion beam assisted deposition (IBAD) method," *Electrochim. Acta*, vol. 54, pp. 6756–6766, 2009.

[55]     E. J. Taylor, E. B. Anderson, and N. R. K. Vilambi, "Preparation of High-Platinum-Utilization Gas Diffusion Electrodes for Proton-Exchange-Membrane Fuel Cells," Electrochemical Society Letters, vol. 139, pp. 45–46, 1992.

[56]     M. W. Verbrugge, "Selective Electrodeposition of Catalyst within Membrane-Electrode Structures," *J. Electrochem. Soc.*, vol. 141, pp. 46, 1994.

[57]     N. Rajalakshmi and K. Dhathathreyan, "Nanostructured platinum catalyst layer prepared by pulsed electrodeposition for use in PEM fuel cells," *Int. J. Hydrogen Energy*, vol. 33, pp. 5672–5677, 2008.

[58]     Y. Ra, J. Lee, I. Kim, S. Bong, and H. Kim, "Preparation of Pt–Ru catalysts on Nafion bonded carbon layer using galvanostatic pulse electrodeposition for proton-exchange membrane fuel cell," *J. Power Sources*, vol. 187, pp. 363–370, 2009.

[59]     S. Woo, I. Kim, J. K. Lee, S. Bong, J. Lee, and H. Kim, "Preparation of cost-effective Pt–Co electrodes by pulse electrodeposition for PEMFC electrocatalysts," *Electrochim. Acta*, vol. 56, pp. 3036–3041, 2011.

[60]     S. Bhattacharjee and M. Secanell, "Effect Of Ionomer Loading in Inkjet Printed Catalyst Coated Membranes On Pefc Performance," Proceedings of the ASME 2012 10th Fuel Cell Science, Engineering and Technology Conference. pp. 1–6, 2012.

[61]     M. S. Saha, "Preparation of Ultra-Thin Catalyst Layers by Piezo-electric Printer for PEMFCs Applications," *ECS Transactions,* vol. 25, no. 1, pp. 2049–2059, 2009.

[62]     S. Towne, V. Viswanathan, J. Holbery, and P. Rieke, "Fabrication of polymer electrolyte membrane fuel cell MEAs utilizing inkjet print technology," *J. Power Sources*, vol. 171, pp. 575–584, 2007.

[63]     A. D. Taylor, E. Y. Kim, V. P. Humes, J. Kizuka, and L. T. Thompson, "Inkjet printing of carbon supported platinum 3-D catalyst layers for use in fuel cells," *J. Power Sources*, vol. 171, pp. 101–106, 2007.

[64]    H. Yu, J. M. Roller, W. E. Mustain, and R. Maric, "Influence of the ionomer/carbon ratio for low-Pt loading catalyst layer prepared by reactive spray deposition technology," *J. Power Sources*, vol. 283, pp. 84–94, 2015.

[65]    Z. Poltarzewski, "Nafion Distribution in Gas Diffusion Electrodes for Solid-Polymer-Electrolyte-Fuel-Cell Applications," *J. Electrochem. Soc.*, vol. 139, pp. 761, 1992.

[66]    M. Uchida, Y. Aoyama, N. Eda, and A. Ohta, "Investigation of the Microstructure in the Catalyst Layer and Effects of Both Perfluorosulfonate Ionomer and PTFE-Loaded Carbon on the Catalyst Layer of Polymer Electrolyte Fuel Cells," vol. 142, 1995.

[67]    E. Antolini, L. Giorgi, a. Pozio, and E. Passalacqua, "Influence of Nafion loading in the catalyst layer of gas-diffusion electrodes for PEFC," *J. Power Sources*, vol. 77, pp. 136–142, 1999.

[68]    E. Passalacqua, F. Lufrano, G. Squadrito, a. Patti, and L. Giorgi, "Nafion content in the catalyst layer of polymer electrolyte fuel cells: Effects on structure and performance," *Electrochim. Acta*, vol. 46, pp. 799–805, 2001.

[69]    P. Gode, F. Jaouen, G. Lindbergh, A. Lundblad, and G. Sundholm, "Influence of the composition on the structure and electrochemical characteristics of the PEFC cathode," *Electrochim. Acta*, vol. 48, pp. 4175–4187, 2003.

[70]    G. Sasikumar, J. . Ihm, and H. Ryu, "Dependence of optimum Nafion content in catalyst layer on platinum loading," *J. Power Sources*, vol. 132, pp. 11–17, 2004.

[71]    A. F. Routh, "Drying of thin colloidal films.," *Rep. Prog. Phys.*, vol. 76, 046603, 2013.

[72]    W. Han and Z. Lin, "Learning from 'coffee rings': ordered structures enabled by controlled evaporative self-assembly," *Angew. Chem. Int. Ed. Engl.*, vol. 51, pp. 1534–46, 2012.

[73]    R. D. Deegan, O. Bakajin, and T. F. Dupont, "Capillary flow as the cause of ring stains from dried liquid drops," *Nature,* pp. 827–829, 1997.

[74]    R. D. Deegan. "Deposition at Pinned and Depinned Contact Lines: Pattern Formation and Applications." Ph.D. University of Chicago. USA, 1998.

[75]    R. D. Deegan, "Pattern formation in drying drops," *Phys. Rev. E*, vol. 61, pp. 475–485, 2000.

[76]    R. Picknett and R. Bexon, "The evaporation of sessile or pendant drops in still air," *J. Colloid Interface Sci.*, vol. 61, pp. 336–350, 1977.

[77]    H. Hu and R. G. Larson, "Evaporation of a Sessile Drop on a Substrate," *J. Phys. Chem. B*, vol. 106, pp. 1334–1344, 2002.

[78] H. Hu and R. G. Larson, "Analysis of the Microfluid Flow in an Evaporating Sessile Drop," *Langmuir*, vol. 21, pp. 3963–3971, 2005.

[79] H. Hu and R. G. Larson, "Analysis of the Effects of Marangoni Stresses on the Microflow in an Evaporating Sessile Drop," Langmuir, 21 (9), pp. 8271–8279, 2005.

[80] H. Hu and R. G. Larson, "Marangoni effect reverses coffee-ring depositions.," *J. Phys. Chem. B*, vol. 110, pp. 7090–4, 2006.

[81] W. Ristenpart, P. Kim, C. Domingues, J. Wan, and H. Stone, "Influence of Substrate Conductivity on Circulation Reversal in Evaporating Drops," *Phys. Rev. Lett.*, vol. 99, pp. 234502, 2007.

[82] R. Bhardwaj, X. Fang, and D. Attinger, "Pattern formation during the evaporation of a colloidal nanoliter drop: a numerical and experimental study," *New J. Phys.*, vol. 11, pp. 075020, 2009.

[83] R. Bhardwaj, J. P. Longtin, and D. Attinger, "Interfacial temperature measurements, high-speed visualization and finite-element simulations of drop impact and evaporation on a solid surface," *Int. J. Heat Mass Transf.*, vol. 53, pp. 3733–3744, 2010.

[84] A. D. Nikolov and D. T. Wasan, "Mechanisms of the Assembly of Nano- and Microparticle Two-Dimensional Structures in a Wedge Film," *Ind. Eng. Chem. Res.*, vol. 48, pp. 2320–2326, 2009.

[85] W. Zhang, T. Yu, L. Liao, and Z. Cao, "Ring formation from a drying sessile colloidal drop," *AIP Adv.*, vol. 3, pp. 102109, 2013.

[86] L. Morales, J. Parlange, M. Wu, F. J. Pe, W. Zhang, W. Sang, and T. S. Steenhuis, "Surfactant-Mediated Control of Colloid Pattern Assembly and Attachment Strength in Evaporating Drops," *Langmuir,* 29 (6), pp 1831–1840, 2013.

[87] T. Still, P. J. Yunker, and A. G. Yodh, "Surfactant-induced Marangoni eddies alter the coffee-rings of evaporating colloidal drops.," *Langmuir*, vol. 28, pp. 4984–8, 2012.

[88] E. Senses, M. Black, T. Cunningham, S. a Sukhishvili, and P. Akcora, "Spatial ordering of colloids in a drying aqueous polymer drop.," *Langmuir*, vol. 29, pp. 2588–94, 2013.

[89] B. M. Weon and J. H. Je, "Fingering inside the coffee ring," *Phys. Rev. E*, vol. 87, pp. 13003, 2013.

[90] P. J. Yunker, T. Still, M. a Lohr, and a G. Yodh, "Suppression of the coffee-ring effect by shape-dependent capillary interactions.," *Nature*, vol. 476, pp. 308–11, 2011.

[91] Y.-F. Li, Y.-J. Sheng, and H.-K. Tsao, "Evaporation stains: suppressing the coffee-ring effect by contact angle hysteresis.," *Langmuir*, vol. 29, pp. 7802–11, 2013.

[92]   a Crivoi and F. Duan, "Elimination of the coffee-ring effect by promoting particle adsorption and long-range interaction.," *Langmuir*, vol. 29, pp. 12067–74, 2013.

[93]   M. Tembely, A. Mercier, C. Nayoze, and A. Soucemarianadin, "Binary-Mixture Drop Evaporation : Lubrication Approximation and Coffee Ring Formation 2 . Model Equation of Motion," *3rd Micro and Nano Flows Conference*, pp. 22–24, 2011.

[94]   Lucas Goehring, "Coffee-ring effect," http://www.lgoehring.com/Coffee-ring_effect.html

[95]   W. Ristenpart, P. Kim, C. Domingues, J. Wan, and H. Stone, "Influence of Substrate Conductivity on Circulation Reversal in Evaporating Drops," *Phys. Rev. Lett.*, vol. 99, pp. 234502, 2007.

[96]   D. de Gennes, Pierre-Gilles, and Brochard-Wyart, Francoise, and Quere, *Capillarity and Wetting Phenomena: Drops, Bubbles, Pearls, Waves*. New York: Springer-Verlag, 2004.

[97]   J.-Y. Ruzicka, "An introduction to ImageJ: Particle Sizing using ImageJ." [Online]. Available: http://mesa.ac.nz/mesa-resources/technical-tutorials/particle-sizing-using-imagej/.

[98]   L. E. Scriven, "The Marangoni Effects," *Nature*, vol. 187, pp. 186–188, 1956.

[99]   B. Sobac and D. Brutin, "Thermocapillary instabilities in an evaporating drop deposited onto a heated substrate," *Phys. Fluids*, vol. 24, pp. 032103, 2012.

[100] K. Sefiane, J. R. Moffat, O. K. Matar, and R. V. Craster, "Self-excited hydrothermal waves in evaporating sessile drops," *Appl. Phys. Lett.*, vol. 93, pp. 074103, 2008.

# Appendix A

Procedure of the image processing: Using Matlab, the sample images are taken by sliding windows along the white dash line (Fig. 5.7), then the image bar is divided into several squares. For sample with different composition, the size of the window varies slightly, make sure the number of windows can be around 50 to ensure the precision of the result. For each square, ImageJ [6]is used for the post-processing, the details is as follow:

1. Sharpening is applied to increase the quality of the image.

2. Grayscale intensities inversion for the thickness of deposition.

    $I = 255 - Io$, where Io is the original grayscale intensity for each pixel, I is the reverted ones.

3. Linear normalization is applied to stretch the inverted grayscale from 0 to 255.

    $In = (I - Min) * (newMax - newMin)/(Max - Min) + newMin$

    I is the reverted grayscale intensity for each pixel after step 2, Min is the minimum value of I in this image, Max is the maximum value of I in this image, newMax is 255, newMin is 0. I$n$ is the linear normalized grayscale value for each pixel.

4. Averaged inverted grayscale intensity

    $Ave = \sum_1^n I / 255*n$, where n is the number of pixels of each square.

The sample image was processed using "particles analyzer" toolbox in ImageJ for the particle size distribution (PSD) analysis. After the image was discretized into several windows (as shown in Fig. 5.10 (b), the number of the points is 26); then the PSD analysis is performed repeatedly on each window. PSD analysis can be summarized as follows:

---

[6] The website for ImageJ: http://imagej.nih.gov/ij/

First, Convert the image into monochrome (no grayscale conversion) and increase the sharpness of the boundary of the deposition. Shown in Fig. A1, it gives two sampled windows taken nearby the edge and at center, respectively. After the processing, the edge of the C/Pt aggregations are more distinguishable.
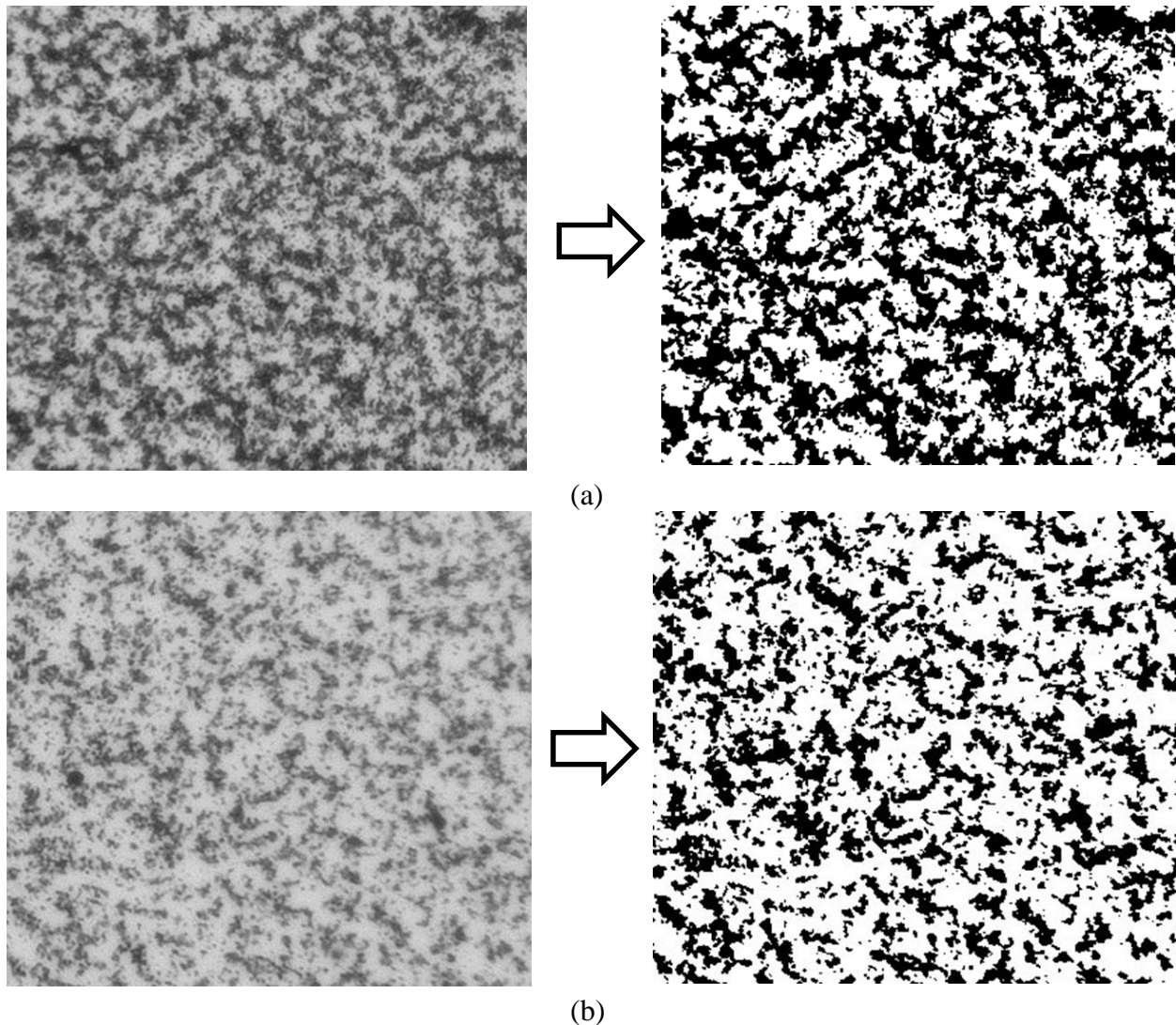


(a)



(b)

Fig A1. Binarization of sample image. (a) The microstructure nearby the edge and its binarized one. (b) The microstructure at the center and its binarized one.

Second, Size particles. This step discretizes the connected C/Pt aggregations into dispersed parts. ImageJ provides automatic particle sizing to discretize C/Pt aggregations based on circularity of the shape of each aggregation. In our case, the shape of C/Pt aggregations are highly irregular,

and usually connected via very narrow bridge (indicated by an arrow in Fig. A2). In order to acquire convincing results, manual particles counting is also provided in ImageJ to cut them into pieces at the narrowing region in advance before the automatic counting. Finally, the area of the each discretized component will be retrieved.



(a)                                        (b)
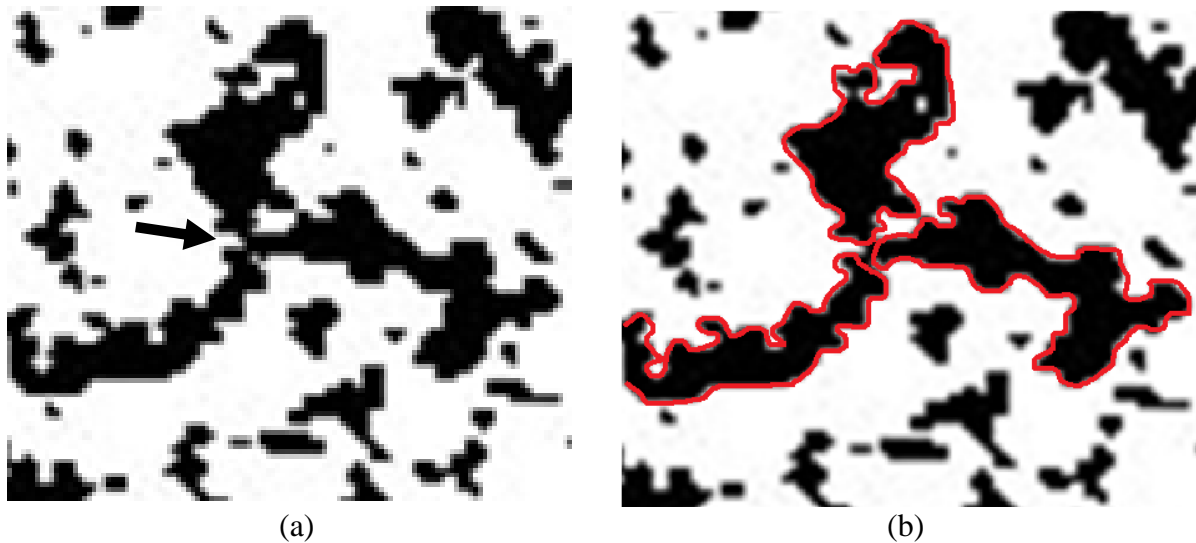
Fig A2. Discretization of connected C/Pt aggregates into dispersed parts. (a) C/Pt aggregations are connected by narrow bridge. (b) Pre-Manual particles counting needs to be performed to cut those aggregations into pieces.

Third, Analyzing particle sizing data using Microsoft Excel. Calculate the equivalent diameter of area of each particle, then count the number of particles of designated diameter range. The PSD of the two sampled image is represented in Fig. 5.10 (a). Each window was performed with the same operation, and particles density of each window is calculated by using the number of the particles being divided by the area of each window (Fig. 5.10 (b)). For more information for the PSD analyzer of ImageJ, the online resource is recommended [97].
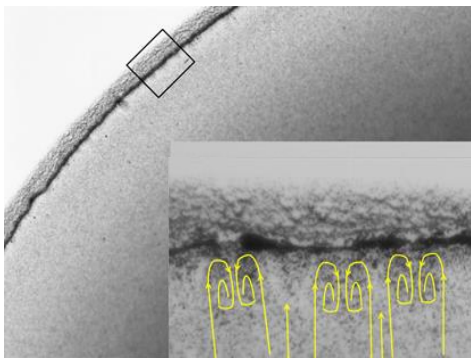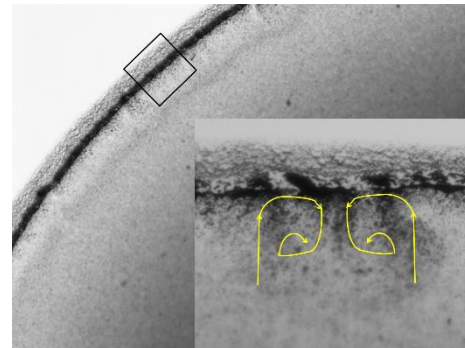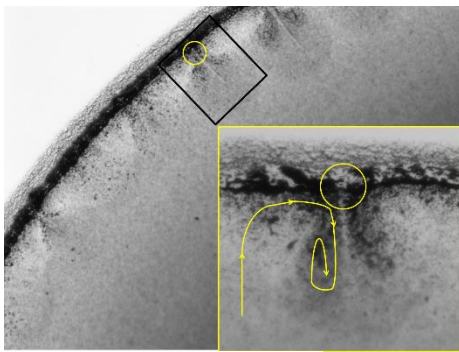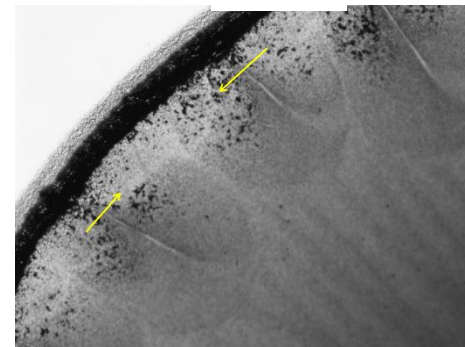
# Appendix B
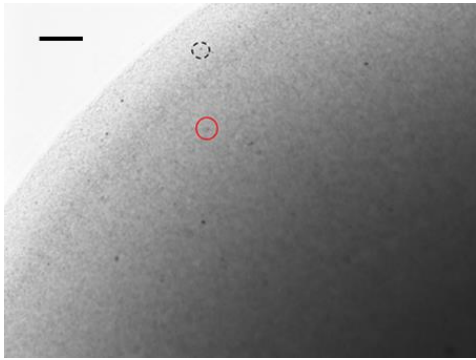


(a)
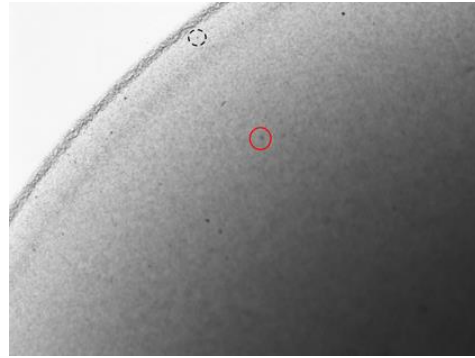
(b)

(c)
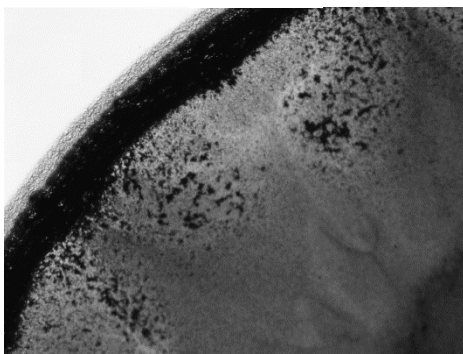
(d)

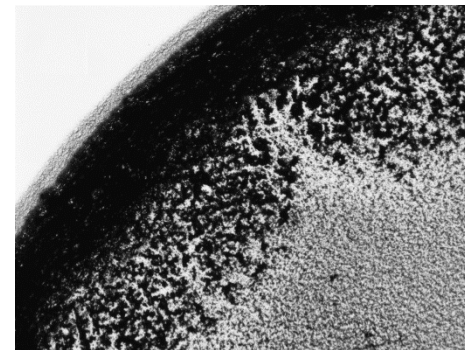(e)

(f)

(g)

(h)

Fig B1. Drying dynamics with focus on edge from initial pinning to final dried out of $W_{Nafion}/W_{Nafion+C/Pt} = 62.5\%$. (a)-> (b), $t \approx 0\ t_{Evap}$, particles flushes toward and pins at the edge, the contact line accrues inward; A reversed flow which bring the particles back toward center is observed; (c) Onset of eddies on the edge, $t \approx 0.05\ t_{Evap}$; the bottom-left image is the magnified one eddy. (d) Faster-growing eddies move together and swallow a slower-growing eddy, to become a pair of larger eddies. $t \approx 0.1\ t_{Evap}$. (e) Formation of a jet-like Marangoni eddy composed of a pair of eddies. $t \approx 0.2\ t_{Evap}$. (f) at $t \approx 0.4\ t_{Evap}$, to (h), Jet-like eddies continues growing, moving, and merging, eventually evolving into larger eddies, and finally dry out to petal-like deposition at the edge. The bar shown in (a) represents 100 μm. $t_{Evap}$ denotes the whole evaporation time.